AWARD NUMBER: W81XWH-19-1-0299

TITLE: Bioinspired Color and Near-Infrared Endoscopy with Affibody Targeted Markers for Colorectal Cancer Surgery

PRINCIPAL INVESTIGATOR: Viktor Gruev

CONTRACTING ORGANIZATION: University of Illinois at Urbana-Champaign

REPORT DATE: Sept 2020

TYPE OF REPORT: Annual

PREPARED FOR: U.S. Army Medical Research and Development Command
Fort Detrick, Maryland 21702-5012

DISTRIBUTION STATEMENT: Approved for Public Release;
Distribution Unlimited

REPORT DOCUMENTATION PAGE

Form Approved
OMB No. 0704-0188

1. REPORT DATE	2. REPORT TYPE	3. DATES COVERED
Sept 2020	Annual	8/15/2019 – 8/14/2020

4. TITLE AND SUBTITLE

Bioinspired Color and Near-Infrared Endoscopy with Affibody Targeted Markers for Colorectal Cancer Surgery

5a. CONTRACT NUMBER

5b. GRANT NUMBER
W81XWH-19-1-0299

5c. PROGRAM ELEMENT NUMBER

5d. PROJECT NUMBER

5e. TASK NUMBER

5f. WORK UNIT NUMBER

6. AUTHOR(S)

Viktor Gruev and Shuming Nie

E-Mail: vgruev@illinois.edu

7. PERFORMING ORGANIZATION NAME(S) AND ADDRESS(ES)

University of Illinois at Urbana-Champaign
GRANTS AND CONTRACTS OFFICE
364 HENRY ADMINISTRATION BLDG
URBANA IL 61801

8. PERFORMING ORGANIZATION REPORT NUMBER

9. SPONSORING / MONITORING AGENCY NAME(S) AND ADDRESS(ES)

U.S. Army Medical Research and Development Command
Fort Detrick, Maryland 21702-5012

10. SPONSOR/MONITOR'S ACRONYM(S)

CDMRP

11. SPONSOR/MONITOR'S REPORT NUMBER(S)

1

12. DISTRIBUTION / AVAILABILITY STATEMENT

Approved for Public Release; Distribution Unlimited

13. SUPPLEMENTARY NOTES

none

14. ABSTRACT

Every year, more than 140,000 people are diagnosed with colorectal cancer (CRC) in the US and about 50,000 succumb to the disease. The Veterans Affairs Central Cancer Registry reports that 3,500 VA patients are diagnosed with CRC and 1,200 will succumb to the disease each year. This abysmal outcome in both civilian and military populations is largely caused by the late diagnosis of CRC, when prognosis is poor. To overcome these health issues, we propose to develop an imaging system capable of simultaneously imaging two affibody peptides labeled with near infrared fluorophores targeting epidermal growth factor receptors, HER1 and HER2 (Aim 2). The proposed technology is broadly applicable to many types of solid tumors, but concerted efforts will be directed toward detection of flat lesions of colitis-associated cancer (CAC and dysplasia. The proposed imaging sensor, based on the evolutionarily honed, highly effective visual system of the mantis shrimp, enables a compact, low-noise, ultra-sensitive device realized by combining vertically stacked photodetectors with pixelated spectral filters (Aim 1). We will optimize two affibody-based molecular agents for simultaneous imaging of different tumor biomarkers and evaluate tumor detection sensitivity and specificity in both small and large animals (Aim 3). We hypothesize that a highly sensitive bioinspired color-fluorescence endoscope, in conjunction with a cocktail of small-sized near-infrared molecular probes for targeted imaging, will detect cancerous and pre-cancerous tissue with high specificity and sensitivity in CRC and CAC patients.

15. SUBJECT TERMS

Endoscopy, near infrared imaging, image guided surgery, colonoscopy

16. SECURITY CLASSIFICATION OF:			17. LIMITATION OF ABSTRACT	18. NUMBER OF PAGES	19a. NAME OF RESPONSIBLE PERSON
a. REPORT	b. ABSTRACT	c. THIS PAGE			USAMRMC
Unclassified	Unclassified	Unclassified	Unclassified		19b. TELEPHONE NUMBER *(include area code)*

TABLE OF CONTENTS

	Page
1. Introduction	1
2. Keywords	1
3. Accomplishments	1
4. Impact	10
5. Changes/Problems	10
6. Products	11
7. Participants & Other Collaborating Organizations	12
8. Special Reporting Requirements	14
9. Appendices	14

1. INTRODUCTION:

Every year, more than 140,000 people are diagnosed with colorectal cancer (CRC) in the US and about 50,000 succumb to the disease. The Veterans Affairs Central Cancer Registry reports that 3,500 VA patients are diagnosed with CRC and 1,200 will succumb to the disease each year. This abysmal outcome in both civilian and military populations is largely caused by the late diagnosis of CRC, when prognosis is poor. To improve early diagnosis, we propose to develop an imaging system capable of simultaneously imaging two affibody peptides labeled with near infrared fluorophores targeting epidermal growth factor receptors, HER1 and HER2. The proposed technology is broadly applicable to many types of solid tumors, but concerted efforts will be directed toward detection of flat lesions of colitis-associated cancer (CAC) and dysplasia. The proposed imaging sensor, based on the evolutionarily honed, highly effective visual system of the mantis shrimp, enables a compact, low-noise, ultra-sensitive device realized by combining vertically stacked photodetectors with pixelated spectral filters. We will optimize two affibody-based molecular agents for simultaneous imaging of different tumor biomarkers and evaluate tumor detection sensitivity and specificity in both small and large animals. We hypothesize that a highly sensitive bioinspired color-fluorescence endoscope, in conjunction with a cocktail of small-sized near-infrared molecular probes for targeted imaging, will detect cancerous and pre-cancerous tissue with high specificity and sensitivity in CRC and CAC patients.

2. KEYWORDS:

colorectal cancer, colitis-associated cancer, near infrared imaging sensors, image guided surgery, minimally invasive surgery, molecular imaging, affibody targeted markers, bioinspired sensors.

3. ACCOMPLISHMENTS:

○ What were the major goals of the project?

The major goals of this project are described in the tables below. We also indicate the progress with each aim and individual tasks within each aim.

Specific Aim 1: Development of a low-noise multispectral imager with high optical density	**Status**
Major Task: To develop and optimize a low-noise, single-chip, bio-inspired multispectral imaging sensor for intraoperative imaging of multiple fluorescent markers	in progress
1.1 Modeling vertically stacked photodiodes.	completed
1.2 Optimizing vertically stacked photodiode and pixel circuitry.	completed
1.3 Optimize layout of the entire image sensor for low noise performance	in progress
1.4 Image sensor fabrication.	1st generation completed; 2nd generation in progress
1.5 Design custom printed circuit board to house imager	completed
1.6 Develop necessary firmware and software to acquire images.	completed
1.7 Model pixelated spectral filter optical performance	completed
1.8 Fabricate pixelated spectral filters	1st generation completed; 2nd generation in progress
1.9 Integrate spectral filters with custom imager.	1st generation completed; 2nd generation in progress
1.10 Evaluate optoelectronic performance of the image sensor.	1st generation completed; 2nd generation in progress

Specific Aim 2: Optimize anti-epidermal growth receptor affibodies for NIR fluorescence imaging	**Status**
Major Task: We will conjugate two anti-EGFR affibody molecules with LICOR fluorophores. The molecular probes will fluoresce in the near infrared spectrum and will target EGF receptors in tumors. The probes will be validated in cell assays.	in progress
2.1 Development of HER-1 targeted affibody marker.	in progress
2.2 Synthesis of HER-2 targeted affibody.	in progress
2.3 Validation of the two affibody targeted probes.	to be started

Specific Aim 3: Imaging colorectal cancer in murine and porcine models	**Status**

Major Task: We will develop colorectal cancer murine and porcine models. The affibody molecular probes will be simultaneously administered to the animal and imaged with our custom-developed endoscope probe.	in progress
3.1 IACUC protocol approval.	approved
3.2 USAMRMC Animal Care and Use Review Office (ACURO) protocol approval.	submitted
3.3 Develop AOM-DSS model for colorectal cancer in mice.	to be started
3.4 Developing orthotopic colorectal cancer mode in mice with HT-29 cell line.	to be started
3.5 System characterization with phantom studies.	in progress
3.6 Fluorescence detection sensitivity, lateral resolution and imaging depth sensitivity.	in progress
3.7 Determination of the specificity and sensitivity of the molecular probe in AOM-DSS CAC/dysplasia and HT-29 mouse models.	to be started
3.8 Determining fluorescence signals in porcine model of CAC.	to be started
3.9 Toxicity and histologic validation.	to be started

- **What was accomplished under these goals?**

Overview: Cancer impacts societies around the world, affecting 1 in 3 people worldwide. While surgery remains the primary curative option for localized cancers, good prognoses require complete removal of the primary tumor and timely recognition of any metastases. To expand surgeons' capabilities and enhance patients' outcomes, we have developed a single-chip color/near-infrared image sensor that mimics the mantis shrimp visual system to enable near-infrared fluorescence image-guidance in both tasks. Just as nature has granted the mantis shrimp with spectral sensitivity at unprecedented optical throughput, data throughput, and spatial resolution, we have supplied our imaging system with six spectral channels by integrating arrays of vertically stacked silicon photodetectors and pixelated spectral filters. To provide information about tumor location that has never before been provided by a single instrument, we have tuned three color channels to provide an intuitive perspective of the surgical procedure and three near-infrared channels to permit multi-functional imaging of optical probes highlighting cancerous tissue and other features characterizing surrounding tissue. In small animal models of human prostate cancer, our image sensor has enabled simultaneous detection of two tumor-targeted fluorophores, distinguishing diseased from healthy tissue in an estimated 99% of all cases, and extraction of near-infrared structured illumination, mapping the surgical site's three-dimensional topography to within 1.2 mm error. That such a simple and compact architecture can offer such flexibility and performance highlights the advantages of biologically inspired sensors over conventionally designed sensors and indicates a path forward for image-guided surgery.

Introduction: Any solution for near-infrared fluorescence image-guided surgery must solve two key problems. The first issue involves architectures: Existing instruments rely on two architectures that are poorly matched to the clinical context. In division-of-time architectures, a filter wheel isolates different spectral channels at different times, permitting all spectral channel to be captured by the same image sensor at distinct timepoints. This collection of spectral information over time requires reduced exposure times with increasing channel counts, maintaining real-time frames rates but reducing the fluorescence's signal-to-noise ratio, and introduces co-registration error between spectral channels due to interframe motion. In division-of-optical-path architectures, dichroic beamsplitters direct different spectral channels along different optical paths, permitting all spectral channels to be captured by distinct image sensors at the same timepoint. This collection of spectral information across space guarantees increased device sizes with increasing channel counts, demanding additional relay optics that impact image quality, while introducing co-registration error between spectral channels as optical elements undergo independent thermal expansion/contraction. The second issue involves feature sets: Existing instruments typically image a single fluorescent probe, providing insufficient sensitivity and specificity to real physiology. Due to variations in inter- and intra-tumor biomarkers, a single tumor-targeted probe may fail to detect metastatic tumors or may fail to detect the boundaries of primary tumors. This is confirmed by a recent meta-analysis that indicates that up to 40% of metastatic tumors and involved lymph nodes can have biomarkers different from those of the primary tumor.

To address these issues, we have taken a radically different approach toward designing a near-infrared fluorescence imaging system—turning to the mantis shrimp visual system as a blueprint for our artificial image sensor. The mantis shrimp benefits from a simple physical phenomenon that imbues spectral sensitivity: Longer-wavelength photons (i.e., red light) penetrate deeper into their compound eyes than shorter-wavelength photons (i.e., blue light) due to a wavelength-dependent absorption coefficient; as a result, the photosensitive cells at the top of their compound eyes preferentially register shorter-wavelength photons, while the photosensitive cells at the bottom preferentially register longer-wavelength photons (Fig. 1a). Crystalline cones above the compound eye provide fine-grained spectral filtering, enabling different parts of the eye to see different bands of light (Fig. 1a). Ultimately, this unique combination of vertically stacked photodetectors with spectral filters enables 16 spatiotemporally-registered spectral bands to be constantly probed by microscopic cells, offering unprecedented benefits: Optical throughput is increased because the vertically stacked structure permits spectral observation without rejecting photons, data throughput is increased because the

vertically stacked structure permits multiple spectral observations at every point, and spatial resolution is increased because spectral observations can be distributed vertically instead of laterally.

A Bio-inspired Image Sensor for Near-Infrared Fluorescence Image-Guided Surgery: To mimic the mantis shrimp's multispectral capabilities, we designed and fabricated an image sensor by monolithically integrating an array of vertically stacked silicon photodetectors with an array of pixelated spectral filters (Fig. 1b). The absorption length of silicon strongly varies with the wavelengths with 99% of blue photons (~400 nm) absorbed within 0.5 μm of penetration and 99% of red photons (~650 nm) absorbed within 16 μm of penetration. Recognizing the high density of photocharge generation by blue photons in a thin sheet near the surface and by red photons in a thick slab below the surface, the location and extent of photodiodes in the silicon can be selected to measure the amounts of blue light and red light in a scene—the blue-sensitive photodiode is shallow and of limited extent, while the red-sensitive photodiode is deeper and of greater extent. Green photons experience an intermediate absorption coefficient and can be detected with an intermediate photodiode. The vertically stacked photodiodes are fabricated by epitaxial growth of three positively-doped silicon layers with individual thicknesses of 0.8 μm, 2.8 μm, and 4.3 μm, followed by ion-implantation to generate negatively-doped regions (Fig. 1b).

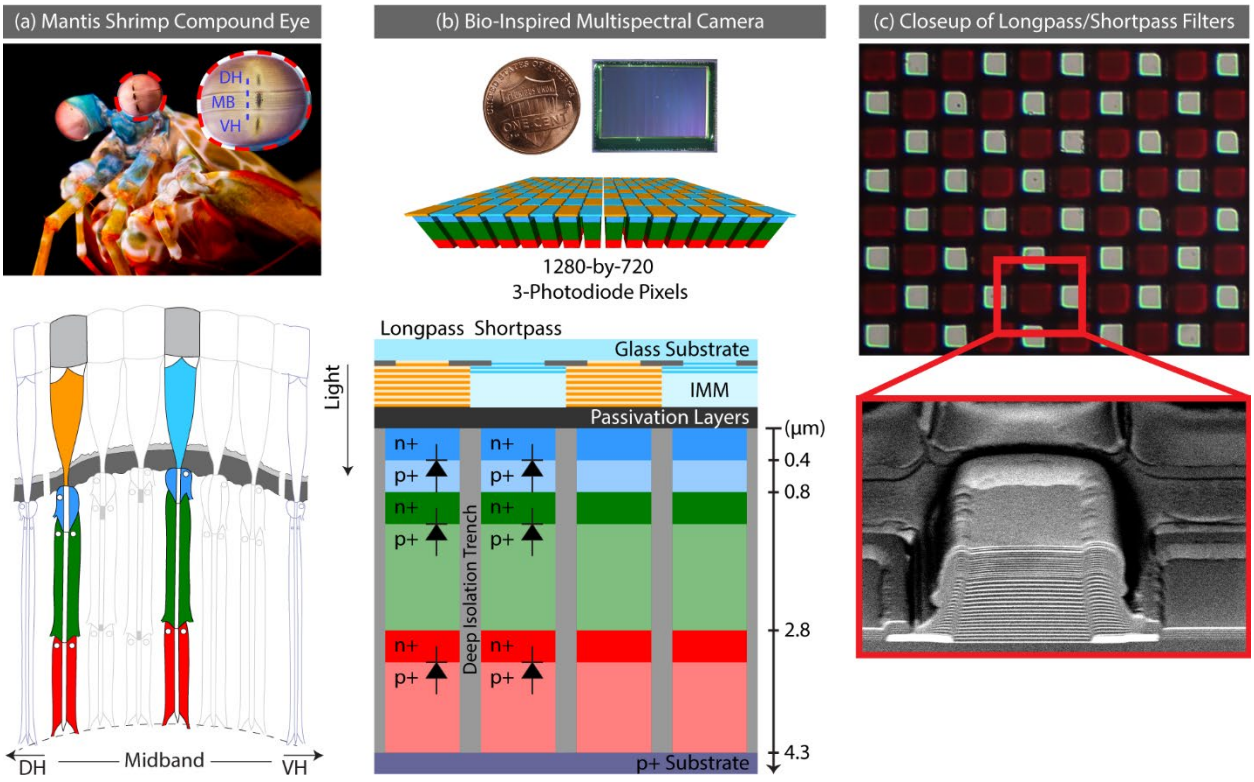

Fig. 1 | Diagrammatic comparison of the mantis shrimp compound eye and our bio-inspired image sensor. The midband section in the mantis shrimp uses a combination of vertically stacked photosensitive cells and spectral filters for spectral discrimination; the addition of reflecting and absorbing pigment reduces optical crosstalk between neighboring rhabdomeres. Similarly, our image sensor uses a combination of pixelated interference filters with chromium lanes and vertically stacked photodetectors with isolation trenches to achieve simultaneous imaging of color and near-infrared light. (a) Close-up views of the stomatopod *Odontodactylus scyllarus*'s compound eye (top) and a cross-sectional diagram of generalized stomatopod ommatidia (bottom). (b) Micrograph and diagrammatic representation of our imager (top) and a cross-sectional diagram showing the combination of pixelated filters and vertically stacked photodiodes (bottom). (c) Optical microscope image of the pixelated optical filters showing the long-pass filters in dark red and the short-pass filters in bright white (top), and a scanning electron microscope image of a long-pass filter in the center and short-pass filters on both sides (bottom). The following abbreviations are used: dorsal hemisphere (DH), index-matching material (IMM), midband (MB), ventral hemisphere (VH).

The array of pixelated spectral filters is produced by stacking submicron layers of silicon dioxide, silicon nitride, and hafnium oxide in different quantities and thicknesses on a glass substrate (Fig. 1c). Organized in an alternating grid of short-pass filters (with passband below 700 nm) and long-pass filters (with passband above 700 nm), the filters provide high in-band transmission (~95%)

and high out-of-band rejection (optical density ~4) (Fig. 2a). The monolithically integrated image sensor is produced by flip-chip bonding the arrays of vertically stacked silicon photodetectors and pixelated spectral filters (Fig. 1b). The three photodiode layers under the short-pass filters maintain distinct spectral responses that peak under blue light, green light, and red light, while the three photodiode layers under the long-pass filters exhibit similar spectral responses that peak at ~700 nm (Fig. 2b); nonetheless, the differences in the spectral responses of the photodiode layers are substantial enough to enable three different observations of the near-infrared spectrum. Together, the three visible channels under the short-pass filters and the three near-infrared channels under the long-pass filter account for a total of six spectral channels—providing hexachromatic vision. As needed, additional notch filters (optical density >6) are placed over the whole sensor to suppress photons from the excitation light source.

Optoelectronic Characterization: When compared against scientific cameras optimized for color reproduction, the stacked photodiodes' spectral responses compare favorably, with the peak wavelengths of Teledyne QImaging's MicroPublisher 6's color channels (i.e., 454 nm, 533 nm, and 606 nm) falling near the peak wavelengths for our imaging system's color channels (i.e., 430 nm, 550 nm, and 670 nm) (Fig. 2b). This correspondence is confirmed in color images where complex natural scenes with diverse color content appear natural. The optimization toward broadly-shaped quantum efficiencies in the visible spectrum ensures sufficient shaping in the spectral responses at the shorter end of the near-infrared spectrum, ensuring that the FDA-approved fluorescent dyes methylene blue ($\lambda_{em} \approx 690$ nm) and indocyanine green ($\lambda_{em} \approx 810$ nm) induce different signals. Furthermore, the location and the extent of the bottom photodiode offer a benefit in the near-infrared spectrum where the quantum efficiency is 50% at 700 nm (Fig. 2b), providing a meaningful increase for weak fluorescent signals at the expense of a computationally-correctable red hue in color images. Further tuning of the photodiode parameters enables an application-specific trade-off between color accuracy and near-infrared discrimination when the selected parameters prove insufficient, all while maintaining the additional benefits to spatial resolution, data throughput, and optical throughput thanks to the stacked photodiodes and filter-less geometry.

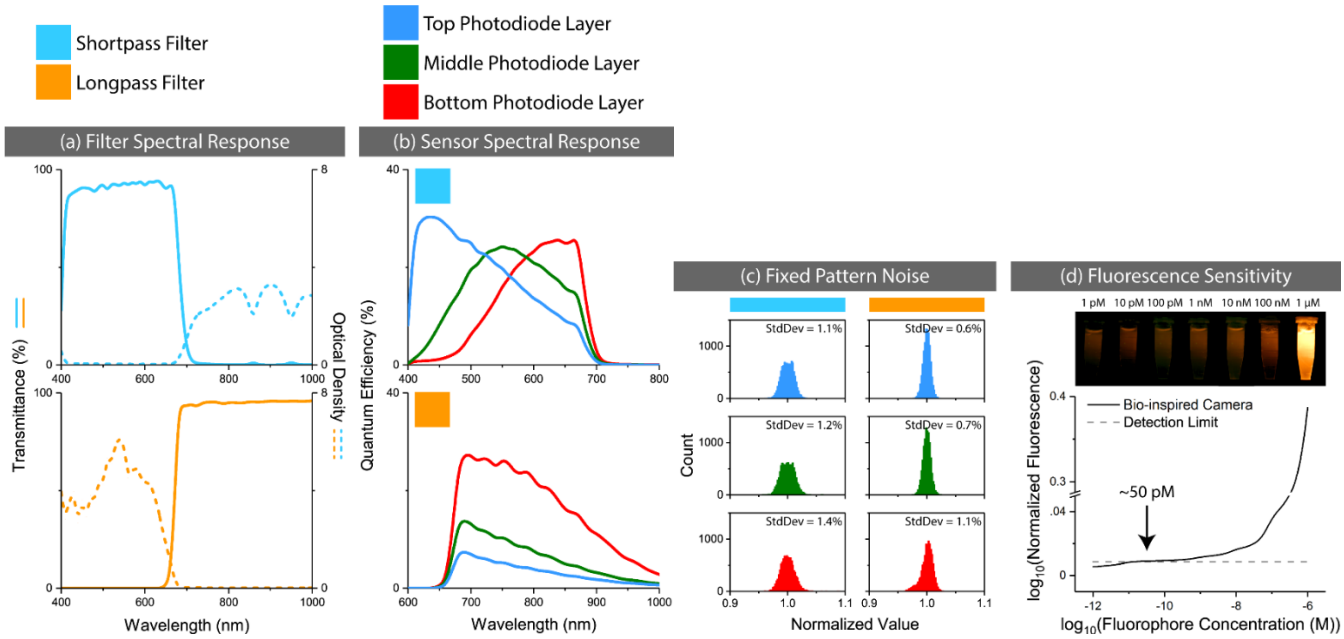

Fig. 2 | Optoelectronic characteristics of our bio-inspired imager. (a) Transmission and optical density curves for our short-pass filters (top, blue) and long-pass filters (bottom, orange). (b) Quantum efficiency curves for the three photodiode layers under the short-pass filters (top) and long-pass filters (bottom). (c) Fixed pattern noise histograms for the three photodiode layers under the short-pass filters (left) and long-pass filters (right). (d) Plot of normalized fluorescence response versus indocyanine green fluorophore concentration where dashed line indicates the detection limit. The minimal detectable concentration of our sensor is 50 pM.

The image sensor exhibits an average read noise of ~70 electrons and an average dark current of ~182 electrons per second. With regard to readout noise, difference double sampling has been implemented in the readout circuitry to mitigate threshold voltage variation across the imaging array at the price of an effective doubling of the read noise. An additional charge-transfer transistor, a pinning layer, and a floating diffusion for each photodiode would permit correlated double sampling which would achieve offset correction at lower noise as demonstrated with scientific CMOS fabrication processes using embedded photodiodes. With regard to dark current, image-guided surgery requires real-time frame rates of ~25 frames per second (<40 milliseconds per frame), limiting the quantity of dark charge that can be accumulated and the power of dark noise that can be observed. Therefore, image sensor

cooling yields a minimal reduction in an already small dark current, producing little improvement in the accumulated dark charge, the observed dark noise, and the resulting signal-to-noise ratio. A fixed-pattern noise of 1.4% is maintained due to difference double sampling in the imager circuitry and high uniformity between the spectral filters (Fig. 2c). The quantum efficiencies coupled with this noise performance permit detection of 50 pM of indocyanine green fluorescence under 20 mW/cm^2 of 780 nm laser excitation (Fig. 2d).

Intraoperative imaging requires simultaneous recordings of weak fluorescence photons, which highlight the location of tumors, and bright visible spectrum photons outlining the patient's anatomical features. Visible photons from the surgical lighting undergo a single reflection at the surface of the surgical site before entering the imaging system, whereas near-infrared photons from the fluorescence excitation undergo a complex series of scattering, absorption, excitation, and emission events before collection, ensuring that the fluorescent photons experience far more losses than the visible photons. However, the International Electrotechnical Commission has specified a lower bound on the illuminance of surgical lighting and an upper bound on the irradiance of fluorescence excitation that prevents changes to the light sources sufficient to overcome losses. The asymmetries in both the optical paths and the lighting specifications conspire to produce a large dynamic range between the strong visible lighting and the weak fluorescent signal that exceeds ~90 dB in the best-case, beyond the 80-dB capability of state-of-the-art sensors. Even if sufficiently large dynamic ranges could be achieved in conventional sensors, e.g., by reducing the readout noise and increasing the full well depth, the requirement that the color image remain unsaturated would practically guarantee that the near-infrared image would occupy the lower half of the dynamic range. Due to the Poisson distribution of the shot noise, the signal-to-noise ratio of the near-infrared image would be minimal, increasing the risk that weakly-labeled fluorescent targets may not be detected. As a result, our image sensor has programmable readout circuitry that independently controls the exposure times for the color pixels and near-infrared pixels. This enables our image sensor to simultaneously acquire high signal-to-noise-ratio images in both the visible and near-infrared spectra.

Tumor Detection in a Small Animal Model of Human Prostate Cancer: To evaluate the sensitivity to multiple fluorophores observed in benchtop experiments within a surgical context, our imaging system was used to identify fluorescently-labeled tumors in a small animal model of human prostate cancers. At the beginning of the study, human prostate cancer cells (LNCaP and PC3) were subcutaneously implanted in nude athymic mice, and ~2 weeks later, two near-infrared fluorescent optical probes (IRDye® 680RD EGF labelled with human recombinant epidermal growth factor and IRDye® 800CW 2-DG labelled with 2-deoxy-D-glucose) were intravenously injected into the same mice. After a ~24-hour delay, the whole mice were fluorescently imaged with our imaging system before the tumor tissue and healthy tissue were surgically removed and separately imaged. Imaging occurred under 665 nm excitation (targeting IRDye® 680RD), 780 nm excitation (targeting IRDye® 800CW), and mixed 665 nm-780 nm excitation (targeting both IRDye® 680RD and IRDye® 800CW).

Using the near-infrared information from our imaging system, each tissue sample was scored and classified as either tumor tissue or healthy tissue, and these predictions were compared against the ground truth. The results of this analysis are detailed in the receiver operating characteristic curves shown in Fig. 3a where an area under the curve of 0.99 can be observed under mixed 665 nm-780 nm excitation (IRDye® 680RD EGF and IRDye® 800CW 2-DG together) compared to 0.83 for 665 nm excitation (IRDye® 680RD EGF alone) and 0.87 for 780 nm excitation (IRDye® 800CW 2-DG alone). Accounting for the paired design of the imaging study, it can be shown that a dual-tracer strategy using EGF and 2-DG together significantly outperforms the single-tracer use of EGF ($p = 0.019$) and the single-tracer use of 2-DG ($p = 0.020$) when comparing areas under the curve. Indeed, the 95% confidence interval for the difference between areas under the curves for the EGF/2-DG scenario and the EGF scenario is (0.04, 0.32), and the same confidence interval for the difference between areas under the curves for the EGF/2-DG scenario and the 2-DG scenario is (0.04, 0.27), indicating a statistically significant improvement in tumor scoring.

All three visible channels are required for color imaging of the surgical site, while two near-infrared channels are required for near-infrared imaging of the fluorescent dyes (IRDye 680RD with $\lambda_{em} \approx 693$ nm and IRDye 800CW with $\lambda_{em} \approx 780$ nm)—accounting for five of the image sensor's spectral channels. The third near-infrared channel is dedicated to three-dimensional reconstruction using structured illumination from a near-infrared projector (at $\lambda \approx 900$ nm)—ensuring full use of all six channels. The projector illuminates the surgical site with a sinusoidal pattern advancing along the wavefront normal, while an algorithm compares the phase change that is observed to the phase change that is expected and extracts the phase change induced by the three-dimensional topography; an inverse model then facilitates conversion of these phase changes into a height map. These three-dimensional reconstructions can be generated at a spatial resolution of 1280 by 720 pixels and a frame rate of 30 frames per second while exhibiting an average root-mean-square error of 1.179 mm and an average signal-to-noise ratio of 36.

Representative images of a mouse before surgery showing both the fluorescently-labeled tumors and the three-dimensional reconstruction are provided in Fig. 3b-d. As measured by our image sensor, the two different fluorescent probes exhibit preferences for the two different tumors, improving tumor detection despite inter-tumor variation, while the three-dimensional information indicate the size and extent of the tumors, offering additional information during surgical resection.

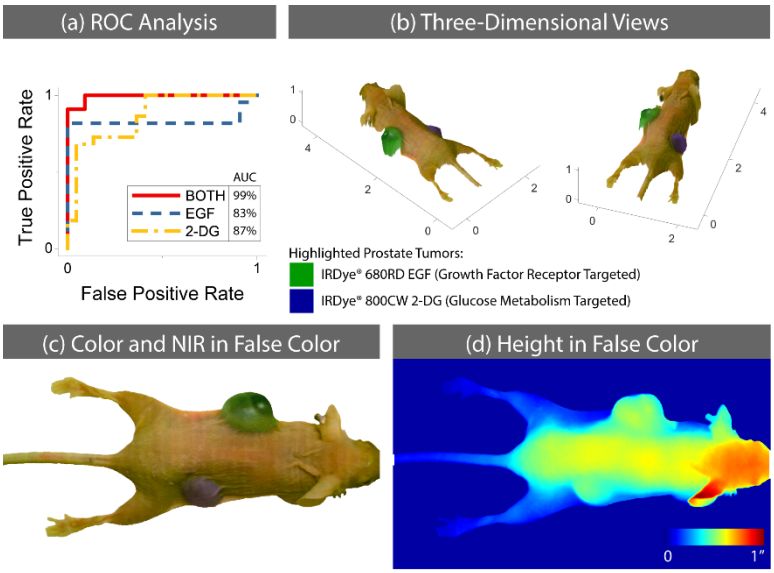

Fig. 3 | Animal study with our bio-inspired imaging sensor to detect tumors using IRDye® 680RD EGF and IRDye® 800CW 2-DG. (a) Receiver operating characteristic curves for tumor detection using both dyes together and each dye alone. Area under the curve is improved to 99% when both targeted probes are used for tumor detection. (b) Two views of a mouse showing the estimated three-dimensional profile and the tumors highlighted with different targeted probes (see Supplementary Video 1). The tumors have an obvious size and extent within the three-dimensional topography, and the different tumors were preferentially labeled by different dyes. (c) Color/near-infrared image of a mouse showing the tumors highlighted with different targeted probes. (d) Three-dimensional profile of a mouse indicating the out-of-plane height. The following abbreviations are used: area under the curve (AUC), near-infrared (NIR), receiver operating characteristic (ROC).

Discussion: When successfully translated to the medical field, new sensing technologies can decrease a patient's medical expenses, increase a patient's quality of life, and directly impact our economy and society. In most hospitals, the primary sensing modalities during surgical procedures are the surgeon's eyesight and touch, leading to subjective discrimination between cancerous and healthy tissues; therefore, there has been intense interest in and numerous proposals for imaging systems that can eliminate the positive tumor margins associated with tumor regrowth and the overly negative tumor margins associated with iatrogenic effects. Unfortunately, imaging technologies have faced little success being adopted into the operating room; the imaging architectures that have come to dominate within the last 50 years of semiconductor and optical research have produced biomedical imaging systems that are incompatible with the clinical environment and lack diagnostic performance.

In this work, we have presented a bio-inspired image sensor with hexachromatic vision for image-guided surgical applications. The sensor, which is realized by monolithically integrating an array of vertically stacked photodetectors with an array of pixelated spectral filters, enables the differentiation of multiple fluorophores across a surgical site and in real time, providing physicians with the critical information required to make surgery-time decisions and enhance surgical outcomes. Near-infrared images are inherently co-registered with visible images in both time and space, eliminating the ambiguity between anatomical features and fluorescently-labeled structures that can turn a perfect incision into a poor prognosis. Tumor detection in small animal models of human prostate cancer indicate that this technology can improve the accuracy of resection as tumor-targeted markers enter clinical practice, while sentinel lymph node detection in patients with breast cancer suggests that this technology can already play a role in providing surgeons with spectral information. With these imaging capabilities, plus a compact footprint and low weight that can be seamlessly integrated into space-constrained operating rooms, our bio-inspired imager can open unprecedented opportunities for quality-based healthcare in both resource-limited and resource-rich hospitals.

- **What opportunities for training and professional development has the project provided?**
  - Two undergraduate students were involved in the project. Both students were mentored by graduate students and the PI for the project.
  - The graduate students involved in this project presented results at several international conferences, such as IEEE International Symposium on Circuits and Systems and SPIE BIOS.

- **How were the results disseminated to communities of interest?**

- The results from this research were presented at several international conferences such as: IEEE International Symposium on Circuits and Systems and SPIE BIOS.
- We also have a journal manuscript in review where we describe our results related to the bio-inspired image sensor.

o What do you plan to do during the next reporting period to accomplish the goals?

During the next reporting period, we will focus on three distinct areas. First, we will focus in integrating our bio-inspired image sensor with an endoscope and evaluate its optical performance. The bio-inspired sensor has been successfully designed and its optical performance has been validated. Hence the integration of the image sensor and endoscope will be straight forward and would enable us to start with the animal cancer models. Second, we will complete the conjugation of the two affibody peptides labeled with near infrared fluorophores targeting epidermal growth factor receptors, HER1 and HER2. Once the two probes have been successfully designed, we will perform various optical test using the custom bio-inspired sensor and endoscope. Third, we will evaluate the overall performance of both endoscopy and NIR molecular probes in animal models of prostate cancer.

4. IMPACT:

o What was the impact on the development of the principal discipline(s) of the project?

Image-guided surgery (IGS) can improve the patient's outcome by providing meaningful real-time information about the location of cancerous tumors and surrounding tissue, aiding in the elimination of positive tumor margins and reducing iatrogenic damage. However, the clinical need for imaging systems that can provide real-time feedback under real operating room settings remains unmet. State-of-the-art imaging systems for near-infrared fluorescence IGS rely on a series of complex optics and several imaging sensors. As a result, these systems are bulky and expensive, and their architecture lacks the versatility to simultaneously image multiple fluorophores, effectively making them cumbersome when merged into the current surgical workflow.

To address these shortcomings, we have designed a multi-spectral imager capable of spatially co-registered hexachromatic vision: three spectral channels in the visible spectrum for the identification of anatomical features in color and three spectral channels in the near-infrared spectrum for the simultaneous identification of multiple near-infrared fluorescence dyes used in IGS. Our single-chip imaging sensor combines the vertically stacked photodetectors technology with pixelated interference filters to create a multi-spectral imager that can help surgeons make clinically relevant decisions in real time, with an effective resolution of 1280x720x3 photodiodes and a frame rate of 24 FPS. Our imager has the ability to identify different shades of near-infrared fluorescent light, allowing the surgeon to use and differentiate multiple fluorophores as molecular probes with high sensitivity and accurately locate tumors.

o What was the impact on other disciplines?

Our paradigm shift imaging sensor can capture both color and NIR information. This information can be used in various other filed beyond the medical filed, such as agriculture and crop monitoring, remote sensing and defense applications. We are also exploring how we can use this sensor to enable safer driving in the truck industry. We will leverage the NIR channel to detect obstacle that otherwise can go unnoticed when driving though adverse conditions.

o What was the impact on technology transfer?

Nothing to Report

o What was the impact on society beyond science and technology?

The potentials for our imaging technology to impact society at large are enormous. We have demonstrated in animal models that our imaging technology has higher sensitivity and specificity in detecting cancerous cells than state of the art imaging instruments. This can lead to better surgical outcome when this technology is clinically translated: the surgical time can be decreased because our technology can enable faster identification of cancerous cells during surgery and it can also ensure complete removal of all cancerous cells. Hence, the overall cost of surgical procedures can be decreased, and we can prevent secondary surgeries by identifying all cancerous cells during the first surgery. This can lead to lower healthcare costs and better quality of life for the patient.

5. CHANGES/PROBLEMS:

o Changes in approach and reasons for change

Nothing to Report

- **Actual or anticipated problems or delays and actions or plans to resolve them**

Due to the COVID-19 pandemic, the students and PI involved in this project had to complete lot of the research activities remotely and away from the University labs. Even though we made good progress during this period, some of the research activity were slowed down or delayed. Currently we have limited access to the lab resources due to University regulations. Students are continuing to make progress with their research while working remotely as much as possible.

We have made very good progress with the design and testing of the proposed bio-inspired image sensor because we were able to complete this work remotely. Due to the limited access to the optical lab, we were not able to integrate the proposed sensor with an endoscope and perform the necessary optical tests. Since the lab is reopened with limited capacity since end of June, we have made a schedule for students to access the lab in safely manner so that we can make progress in testing the new imaging system.

The conjugation of the proposed molecular markers was slowed down due to the limited access to the chemistry lab. Furthermore, we had difficulty in recruiting a student to work on the conjugation of the molecular probes. We were able to hire a post doctoral researcher starting July 1st and he is making good progress with the conjugation of the molecular markers. I anticipate that we will be able to make good progress in this are in the next couple of months and start with animal studies by the end of this year. Also, due to the safety protocol introduced in my lab as part of the COVID19 pandemic, we have to limit the number of animal studies so that we can quickly ramp down and terminate a study if the University has to shut down. This restriction will slow down the progress with the animal studies and we will due our best to schedule these studies to minimize any delays.

- **Changes that had a significant impact on expenditures**

We were able to recruit only one graduate student instead of the planned two graduate students to work on this project for the first 10 months of the project. Earlier this summer, we recruited a post-doctoral researcher who will help make the necessary research progress as planned. We have also recruited several undergraduate students to help with the proposed research. Hence, we were not able to spend the allocated money for personal.

We were originally planning to fabricate our proposed spectral filters through Salvotechnology Inc. cleanroom facilities. However, the company has provided free samples of the pixelated spectral filters which we have integrated with our bioinspired sensor. Once we evaluate the performance of the overall system and evaluate any shortcomings, the second generation of filters will be fabricated through the same company. Also Foveon/Sigma have provided free samples of their vertically stacked image sensors which has alleviated some of the planned expenses for the proposed endoscope. We plan to investigate other low noise image sensors with these extra resources to be able to surpass the performance of the proposed instrument.

- **Significant changes in use or care of human subjects, vertebrate animals, biohazards, and/or select agents**

Nothing to Report

- **Significant changes in use or care of human subjects**

Nothing to Report

- **Significant changes in use or care of vertebrate animals.**

Nothing to Report

- **Significant changes in use of biohazards and/or select agents**

Nothing to Report

6. PRODUCTS:

- **Publications, conference papers, and presentations**

- **Journal publications.**

S. Blair, M. Garcia, T. Davis, C. Konopka, K. Kauffman, R. Colanceski, I. Ferati, B. Kondov, S. Stojanovski, M. Bogdanovska Todorovska, N. T. Dimitrovska, N. Jakupi, D. Miladinova, G. Petrusevska, G. Kondov, L. W. Dobrucki, S. Nie, and V. Gruev, "Hexachromatic Bio-inspired Camera for Image-Guided Cancer Surgery", Science Translation Medicine (in review)., acknowledgement of federal support: yes.

- **Books or other non-periodical, one-time publications.**

Anthony Li, "Low Noise CMOS Image Sensors", Master Thesis Dissertation, acknowledgement of federal support: no

- **Other publications, conference papers, and presentations.**

Blair SM, Deliwala A, Chen E, Subashbabu S, Li A, George M, Garcia M, Cui N, Gruev V. "A backside-illuminated low-noise multispectral imager for near-infrared fluorescence image-guided surgery." *International Society for Optics and Photonics, Molecular-Guided Surgery: Molecules, Devices, and Applications*, 2020.

Steven Blair, Nan Cui, Missael Garcia, and Viktor Gruev, "A 140 dB DR Logarithmic Multispectral Imager for Near-Infrared Fluorescence Image-Guided Surgery", *IEEE International Symposium on Circuits and Systems*, 2020. acknowledgement of federal support: yes*

Steven Blair, Amit Deliwala, Eric Chen, Sailesh Subashbabu, Anthony Li, Mebin George, Missael Garcia, Nan Cui, Stefan Andonovski, Borislav Kondov, Sinisa Stojanoski, Magde Todorovska, Gordana Petrusevska, Goran Kondov, Viktor Gruev, "A 4 e^- Read Noise, 74 dB Dynamic Range Backside-Illuminated Multispectral Imager for Near-Infrared Fluorescence Image-Guided Surgery", *IEEE International Symposium on Circuits and Systems*, 2020. acknowledgement of federal support: yes*

7. PARTICIPANTS & OTHER COLLABORATING ORGANIZATIONS

- **What individuals have worked on the project?**

Name:	Viktor Gruev
Project Role:	*Principle Investigator*
Researcher Identifier (e.g. ORCID ID):	
Nearest person month worked:	2
Contribution to Project:	*Oversaw the design of the bio-inspired image sensors, approval of the IACUC protocol, design of the endoscopy system, mentoring graduate and undergraduate students.*

Name:	Shuming Nie
Project Role:	*Co-Principle Investigator*
Researcher Identifier (e.g. ORCID ID):	
Nearest person month worked:	1
Contribution to Project:	*Oversaw the design of the animal studies, oversaw the conjugation of the molecular probes, mentoring graduate and undergraduate students.*

Name:	Zhongmin Zhu
Project Role:	*Undergraduate student*
Researcher Identifier (e.g. ORCID ID):	
Nearest person month worked:	6
Contribution to Project:	*Designed low noise printed circuit boards for bio-inspired image sensor. Developed and tested necessary firmware and software to acquire real-time data from the custom image sensor.*

Name:	Zudong Liang
Project Role:	*Undergraduate student*
Researcher Identifier (e.g. ORCID ID):	
Nearest person month worked:	6
Contribution to Project:	*Designed low noise printed circuit boards for bio-inspired image sensor. Developed and tested necessary firmware and software to acquire real-time data from the custom image sensor. Designed and fabricated camera casings for the image sensor.*

Name:	Tyler Davis
Project Role:	*Undergraduate student*
Researcher Identifier (e.g. ORCID ID):	
Nearest person month worked:	2
Contribution to Project:	*Performed optical evaluation of the image sensor and collected animal data with the proposed sensor.*

Name:	Steven Blair
Project Role:	*Graduate student*
Researcher Identifier (e.g. ORCID ID):	
Nearest person month worked:	2
Contribution to Project:	*Performed optical evaluation of the bio-inspired image sensor. Designed and analyzed data from animal studies to evaluate sensitivity and specificity of the proposed bioinspired sensor. Designed new generation of*

	printed circuit boards for low noise image sensor. Wrote and edited manuscripts.

Name:	Mebin George
Project Role:	*Graduate student*
Researcher Identifier (e.g. ORCID ID):	
Nearest person month worked:	6
Contribution to Project:	*Researched NIR endoscopes and various light sources for the endoscope. Designed animal experiments to evaluate performance of image sensor and molecular probes.*

- **Has there been a change in the active other support of the PD/PI(s) or senior/key personnel since the last reporting period?**

  The NSF grant titled: " Bioinspired Multispectral Imager for Near Infrared Fluorescence Image Guided Surgery" was completed and is no longer active.

  The NSF grant titled: "UV-MultiSpectral-Polarization 3D Imaging of the Underwater World" was completed and is no longer active.

- **What other organizations were involved as partners?**

  Nothing to Report

8. SPECIAL REPORTING REQUIREMENTS

Nothing to Report

9. APPENDICES:

- Copy of our journal manuscript titled: "Hexachromatic Bio-inspired Camera for Image-Guided Cancer Surgery"
- Copy of our conference manuscript titled: "A 140 dB DR Logarithmic Multispectral Imager for Near-Infrared Fluorescence Image-Guided Surgery"
- Copt of our conference manuscript titled: "A 4 e^- Read Noise, 74 dB Dynamic Range Backside-Illuminated Multispectral Imager for Near-Infrared Fluorescence Image-Guided Surgery"

FRONT MATTER

Title: Hexachromatic Bio-inspired Camera for Image-Guided Cancer Surgery

Authors

S. Blair[1], M. Garcia[1], T. Davis[1], C. Konopka[2,3], K. Kauffman[4], R. Colanceski[5], I. Ferati[5], B. Kondov[5], S. Stojanovski[6], M. Bogdanovska Todorovska[7], N. T. Dimitrovska[5], N. Jakupi[5], D. Miladinova[6], G. Petrusevska[7], G. Kondov[5], L. W. Dobrucki[2,3,10], S. Nie[1,2,8,9], and V. Gruev[1,3,10†]

Affiliations

[1] Department of Electrical and Computer Engineering, University of Illinois at Urbana-Champaign, Urbana, IL, USA.
[2] Department of Bioengineering, University of Illinois at Urbana-Champaign, Urbana, IL, USA.
[3] Beckman Institute for Advanced Science and Technology, University of Illinois at Urbana-Champaign, Urbana, IL, USA.
[4] Department of Biomedical Engineering, University of Michigan, Ann Arbor, MI, USA.
[5] University Clinic Hospital, Department of Thoracic and Vascular Surgery, Ss. Cyril and Methodius University of Skopje, Skopje, Republic of North Macedonia.
[6] University Clinic Hospital, Department of Nuclear Medicine, Ss. Cyril and Methodius University of Skopje, Skopje, Republic of North Macedonia.
[7] University Clinic Hospital, Department of Pathology, Ss. Cyril and Methodius University of Skopje, Skopje, Republic of North Macedonia.
[8] Department of Chemistry, University of Illinois at Urbana-Champaign, Urbana, IL, USA.
[9] Department of Materials Science and Engineering, University of Illinois at Urbana-Champaign, Urbana, IL, USA.
[10] Carle Illinois College of Medicine, University of Illinois at Urbana-Champaign, Urbana, IL, USA.

[†]Corresponding Author: vgruev@illinois.edu

Abstract

Cancer impacts societies around the world, affecting 1 in 3 people worldwide. While surgery remains the primary curative option for localized cancers, good prognoses require complete removal of primary tumors and timely recognition of metastases. To expand surgeons' capabilities and enhance patients' outcomes, we have developed a single-chip color/near-infrared image sensor inspired by the mantis shrimp visual system that enables near-infrared fluorescence image guidance in both tasks. Just as nature has granted the mantis shrimp with spectral sensitivity at unprecedented optical throughput, data throughput, and spatial resolution, we have constructed an imaging system with six spectral channels by integrating arrays of vertically stacked silicon photodetectors and pixelated spectral filters. To provide information about tumor location never before available from a single instrument, we have tuned three color channels to provide an intuitive perspective of the surgical procedure and three near-infrared channels to permit multifunctional imaging of optical probes highlighting cancerous tissue and other features characterizing surrounding tissue. In small-animal models of human prostate cancer, our image sensor has enabled simultaneous detection of two tumor-targeted fluorophores, distinguishing diseased from healthy tissue in an estimated 92% of all cases, and extraction of near-infrared structured illumination, mapping the surgical site's three-dimensional topography to within 1.2 mm error. That this simple and compact architecture can offer such flexibility and performance

highlights the advantages of biologically inspired sensors over conventionally designed sensors and indicates a path forward for image-guided surgery.

MAIN TEXT

Introduction

As humans have pursued rapid advancements in digital cameras, we have also found new biomedical applications for those cameras—developing everything from intraoperative imagers guiding surgical resection (*1-4*) to lab-on-a-chip devices identifying pathological samples (*5*). For diseases like cancer, where removal of primary tumors and confirmation of negative margins are critical to treatment, such improvements to surgery and pathology would appear to be a boon; however, there is a notable gap in the translation of many imaging technologies to clinical practice. As an example, near-infrared fluorescence image-guided surgery has shown enormous potential for cancer surgery due to tissue's low autofluorescence and scattering in the near-infrared, enabling large signal-to-background ratios and imaging depths while eschewing damaging ionizing radiation (*6-9*). With spectral sensitivity spanning the visible and near-infrared, it would seem that digital cameras would be well suited to color imaging of the surgical site and near-infrared imaging of fluorescently labeled tumors, but state-of-the-art near-infrared fluorescence imaging systems suffer from complex architectures and narrow feature sets that have hindered adoption of the next generation of tumor-targeted fluorophores, let alone the current stable of nonspecific fluorophores. Even though the first fluorescence image-guided surgery was performed over 70 years ago, these issues have prevented near-infrared fluorescence image-guided surgery from being widely accepted as standard of care, turning most physicians toward sensory devices that are far older: their unaided senses of sight and touch. Unfortunately, human eyes and fingers are simply not optimized to the task: incomplete tumor resection occurs in 25% of patients with breast cancer, 35% of patients with colon cancer, and 40% of patients with head and neck cancer *(10)*. It would seem, then, that the solution to near-infrared fluorescence image-guided surgery lies somewhere between the digital cameras that engineering has wrought and the eyes that biology has created.

The optimization of both manmade digital cameras and naturally evolved eyes has been driven by selection toward maximum fitness. Digital cameras have been developed over a handful of decades to satisfy consumers documenting daily life in real time and at high resolution (*11*), while eyes have evolved over millions of years to facilitate the complex decisions that permit survival of the species (*12*). Such divergent evolutionary pathways have created vastly different visual systems. Engineers have achieved frame rates and spatial resolutions that surpass nature (*13*) while offering quantum efficiencies, dynamic ranges, and signal-to-noise ratios that can be tuned over tremendous ranges. Biology has in turn seized the upper hand with visual systems that detect spectral information with extremely efficient and effective architectures (*14, 15*); for example, the mantis shrimp visual system, which fits 16 types of cone cells onto compact eyestalks, is unmatched by any manmade spectral camera in power consumption and information density. The marriage of the optimized optoelectronics built into digital cameras and the diverse functionality observed in eyes has inspired novel imaging systems with sensory capabilities exceeding those previously provided by engineers and biology alike (*9, 16, 17*), suggesting a path forward for near-infrared fluorescence image-guided surgery.

Results

The Biologically Inspired Solution to an Unmet Clinical Need

Any solution for near-infrared fluorescence image-guided surgery must solve two key problems. The first issue involves architectures: existing instruments rely on two architectures that are poorly matched to the clinical context (Supplementary Tables S1). In division-of-time architectures, a filter wheel isolates different spectral channels at different times, permitting all spectral channels to be captured by the same image sensor at distinct time points. This collection of spectral information over time requires reduced exposure times with increasing channel counts, maintaining real-time frames rates but reducing fluorescence signal-to-noise ratios, and introduces co-registration error between spectral channels due to interframe motion. In division-of-optical-path architectures, dichroic beamsplitters direct different spectral channels along different optical paths, permitting all spectral channels to be captured by distinct image sensors at the same time point. This collection of spectral information across space guarantees increased device sizes with increasing channel counts, demanding additional relay optics that impact image quality, while introducing co-registration error between spectral channels as optical elements undergo independent thermal expansion/contraction (*9*). The second issue involves feature sets: existing instruments typically image a single fluorescent probe (Supplementary Tables S1 and S2), providing insufficient sensitivity and specificity for real physiology. Due to variations in inter- and intratumor biomarkers, a single tumor-targeted probe may fail to detect metastatic tumors or may fail to detect the boundaries of primary tumors. This is confirmed by a recent meta-analysis indicating that up to 40% of metastatic tumors and involved lymph nodes can have biomarkers different from those of the primary tumor (*18*).

To address these issues, we have taken a radically different approach toward designing a near-infrared fluorescence imaging system—turning to the mantis shrimp visual system as a blueprint for our artificial image sensor. The mantis shrimp benefits from a simple physical phenomenon that imbues spectral sensitivity: shorter-wavelength photons (i.e., blue light) penetrate shorter distances into their compound eyes than longer-wavelength photons (i.e., red light) due to a wavelength-dependent absorption coefficient (*19*); as a result, the photosensitive cells at the top of their compound eyes preferentially register shorter-wavelength photons, while the photosensitive cells at the bottom preferentially register longer-wavelength photons (Fig. 1a). Crystalline cones above the compound eye provide fine-grained spectral filtering, enabling different parts of the eye to see different bands of light (Fig. 1a). Ultimately, this unique combination of vertically stacked photodetectors with spectral filters enables 16 spatiotemporally registered spectral bands to be constantly probed by microscopic cells, offering unprecedented benefits: optical throughput is increased because the vertically stacked structure permits spectral observation without rejecting photons, data throughput is increased because the vertically stacked structure permits multiple spectral observations at every point, and spatial resolution is increased because spectral observations can be distributed vertically instead of laterally.

A Bio-inspired Image Sensor for Near-Infrared Fluorescence Image-Guided Surgery

To mimic the mantis shrimp's multispectral capabilities, we designed and fabricated an image sensor by monolithically integrating an array of vertically stacked silicon photodetectors with an array of pixelated spectral filters (Fig. 1b). The absorption length of silicon strongly varies with wavelength, with 99% of blue photons (~400 nm) absorbed within 0.5 μm of penetration and 99% of red photons (~650 nm) absorbed within 16 μm of penetration. Recognizing the high density of photocharge generation by blue photons in a thin sheet near the surface and by red photons in a thick slab below the surface, the location and extent of photodiodes in the silicon can be selected to measure the amounts of blue light and red light in a scene: the blue-sensitive photodiode is shallow and of limited extent, while the red-sensitive photodiode is deeper and of greater extent. Green photons experience an intermediate absorption coefficient and can be detected with an intermediate photodiode. The spectrum of incident photons can be shaped with spectral filters, enabling a wide range of unique responses.

The array of vertically stacked photodiodes is fabricated by epitaxial growth of three positively doped silicon layers with individual thicknesses of 0.8 μm, 2.8 μm, and 4.3 μm, followed by ion implantation to generate negatively doped regions (Fig. 1b). The photodiodes are most responsive at ~430 nm, ~550 nm, and ~700 nm but maintain responsiveness at longer wavelengths. The array of pixelated spectral filters is produced by stacking submicron layers of silicon dioxide, silicon nitride, and hafnium oxide in different quantities and thicknesses on a glass substrate (Fig. 1c). Organized in an alternating grid of short-pass filters (with passband below 700 nm) and long-pass filters (with passband above 700 nm), the filters provide high in-band transmission (~95%) and high out-of-band rejection (optical density ~4) (Fig. 2a). The monolithically integrated image sensor is produced by flip-chip bonding the arrays of vertically stacked silicon photodetectors and pixelated spectral filters (Fig. 1b). The three photodiode layers under the short-pass filters maintain distinct spectral responses that peak under blue light, green light, and red light; the three photodiode layers under the long-pass filters exhibit similar spectral responses that peak at ~700 nm (Fig. 2b), but the differences in the spectral responses of the photodiode layers are substantial enough to enable three different observations of the near-infrared spectrum. Together, the three visible channels under the short-pass filters and the three near-infrared channels under the long-pass filter account for a total of six spectral channels—providing hexachromatic vision. As needed, additional notch filters (optical density >6) are placed over the whole sensor to suppress photons from the excitation light source.

Optoelectronic Characterization

When compared against scientific cameras optimized for color reproduction, the stacked photodiodes' spectral responses compare favorably, with the centroid wavelengths of Teledyne QImaging's MicroPublisher 6's color channels (i.e., 464 nm, 540 nm, and 608 nm) (*20*) falling near the centroid wavelengths for our imaging system's color channels (i.e., 507 nm, 566 nm, and 624 nm) (Fig. 2b). This correspondence is confirmed in color images where complex natural scenes with diverse color content appear natural (Supplementary Fig. S1). The optimization toward broadly shaped quantum efficiencies in the visible spectrum ensures sufficient shaping in the spectral responses at the shorter end of the near-infrared spectrum, ensuring that the FDA-approved fluorescent dyes methylene blue (MB; $\lambda_{em} \approx 690$ nm) and indocyanine green (ICG; $\lambda_{em} \approx 810$ nm) induce different signals. Furthermore, the location and the extent of the bottom photodiode offer a benefit in the near-infrared spectrum where the spectral response doesn't degrade until beyond 1000 nm (Fig. 2b), providing a meaningful increase for weak fluorescent signals at the expense of a computationally correctable red hue in color images. Further tuning of the photodiode parameters enables an application-specific trade-off between color accuracy and near-infrared discrimination when the selected parameters prove insufficient, all while maintaining the additional benefits to spatial resolution, data throughput, and optical throughput thanks to the stacked photodiodes and filterless geometry.

The image sensor exhibits a read noise that is 0.4% of the signal at half full-scale range and a fixed pattern noise that is 0.6% of the signal at half full-scale range (Fig. 2c). Both the read noise and the fixed pattern noise are affected by difference double sampling within the readout circuit: at the price of an effective doubling of the read noise at each pixel, there is a substantial drop in threshold voltage variation across the image sensor. An additional charge-transfer transistor, a pinning layer, and a floating diffusion for each photodiode would permit correlated double sampling, which would simultaneously reduce read noise and correct offsets, as demonstrated in scientific CMOS fabrication processes using embedded photodiodes (*21, 22*). The dark current of the image sensor fills 1.5% of the full-scale range per second, but it should be noted that image-guided surgery requires real-time frame rates of ~25 frames per second (<40 milliseconds per frame), limiting the quantity of dark charge that can be accumulated and the power of dark noise that can be observed. Therefore, common

corrections like image sensor cooling yield a minimal reduction in an already small dark current, producing little improvement in the accumulated dark charge, the observed dark noise, and the resulting signal-to-noise ratio. The quantum efficiencies coupled with this noise performance permit detection of 316 pM of ICG at 200-ms integration time under 20 mW/cm^2 of 780 nm laser excitation (Fig. 2d).

Intraoperative imaging requires simultaneous recording of weak fluorescence photons, which highlight the location of tumors, and bright visible-spectrum photons outlining the patient's anatomical features. Visible photons from the surgical lighting undergo a single reflection at the surface of the surgical site before entering the imaging system, whereas near-infrared photons from the fluorescence excitation undergo a complex series of scattering, absorption, excitation, and emission events before collection, ensuring that the fluorescent photons experience far more losses than the visible photons. However, the International Electrotechnical Commission has specified a lower bound on the illuminance of surgical lighting and an upper bound on the irradiance of fluorescence excitation that prevents changes to the light sources sufficient to overcome losses (*23, 24*). These asymmetries in optical paths and lighting specifications conspire to produce a large dynamic range between the strong visible lighting and the weak fluorescent signal that exceeds ~90 dB in the best case, beyond the 80-dB capability of state-of-the-art sensors. Even if sufficiently large dynamic ranges could be achieved in conventional sensors, for example, by reducing the readout noise and increasing the full well depth, the requirement that the color image remain unsaturated would practically guarantee that the near-infrared image would occupy the lower half of the dynamic range. Due to the Poisson distribution of the shot noise, the signal-to-noise ratio of the near-infrared image would be minimal, increasing the risk that weakly labeled fluorescent targets may not be detected. As a result, our image sensor has programmable readout circuitry that independently controls the exposure times for the color pixels and near-infrared pixels. This enables our image sensor to simultaneously acquire high signal-to-noise-ratio images in both the visible and near-infrared spectra.

Simultaneous Imaging of Multiple Near-Infrared Fluorescent Signals

Since the most important information about the near-infrared spectrum is encoded in the comparative variation across and the overall intensity of the near-infrared channels, not the absolute value of each channel, a transformation is required to map the measured photodiode response to a more intuitive quantity. In practice, the transformation from red-green-blue (RGB) to hue-saturation-value (HSV) used in color image processing has proven adept at separating different signals encoded in the near-infrared channels. Under this transformation, hue and saturation represent ratios of differences between the three channels, providing information about the incident spectrum, while value represents the response of the strongest channel, providing information about the incident intensity. Taken together, hue and saturation enable differentiation of multiple targets (e.g., two fluorescent markers) based on the targets' spectral characteristics (e.g., different emission wavelengths), while value permits a comparison between the targets' intensities. Even without the physical meaning of the total energy across spectral bands, the abstract quantities of hue, saturation, and value permit application-specific descriptions for image-guided surgery while enabling full use of the near-infrared measurements at each pixel.

To demonstrate that the image sensor is sensitive to small perturbations of the incident spectrum, we prepared the near-infrared fluorophore ICG in two different solvents, deionized water and fetal bovine serum. When excited with the same light source, the emission peaks from these samples are spectrally separated by just 8 nm, but the emission spectra from these samples are clearly distinguished by our image sensor, as evidenced by the separation in the 95% tolerance ellipses for the hues and saturations

(Fig. 3a). To illustrate further that the hue-saturation-value response varies continuously with a smooth change in the incident spectrum, we prepared the near-infrared fluorophores IRDye® 680RD and IRDye® 800CW in seven volumetric ratios from 10-to-0 to 0-to-10. When excited with two light sources, the single degree of freedom in volumetric ratios dictates that the emitted spectrum from the fluorophore mixture is the volume-weighted average of the emission spectra from the individual fluorophores; indeed, our image sensor returns hues and saturations confined about a one-dimensional manifold with limited overlap between the 95% tolerance ellipses associated with different ratios (Fig. 3b), permitting quantification of the relative concentrations of the two dyes. Both these results were achieved thanks to the spectral sensitivity, temporal noise performance, and spatial noise performance of the imaging system.

While the image sensor's ability to distinguish emission spectra has notable applications, its ability to differentiate emission spectra from excitation spectra is also important. Since the hue and saturation provide information about the incident spectrum, and since the fluorescent excitation spectrum and the fluorescent emission spectrum are always different, the reflection from an excitation light source and the emission from a fluorophore will map to different hue-saturation points, permitting discrimination in the hue-saturation space. This has applications in surgery, where the small number of excitation photons that reflect from the surgical site and pass through the emission filter compete with the potentially small number of emission photons that reach the image sensor. A divergence in response is exhibited in the benchtop experiment shown in Fig. 3c-g, where pixels exposed only to fluorescence excitation or fluorescence emission lie in separate clusters in the hue-saturation space and pixels exposed to a mixture of excitation and emission lie between. This permits labeling of pixels that are useful (observe mostly emission), useless (observe mostly excitation), and of potential use (observe a mixture of emission and excitation).

Tumor Detection in a Small-Animal Model of Human Prostate Cancer

To evaluate the sensitivity to multiple fluorophores observed in benchtop experiments within a surgical context, our imaging system was used to identify fluorescently labeled tumors in a small-animal model of human prostate cancer. At the beginning of the study, human prostate cancer cells (LNCaP and PC3) were subcutaneously implanted in nude athymic mice, and ~2 weeks later, two near-infrared fluorescent optical probes (IRDye® 680RD EGF labeled with human recombinant epidermal growth factor and IRDye® 800CW 2-DG labeled with 2-deoxy-D-glucose) were intravenously injected into the same mice. After a ~24-hour delay, the whole mice were fluorescently imaged with our imaging system before the tumor tissue and healthy tissue were surgically removed and separately imaged. Imaging occurred under 665 nm excitation (targeting IRDye® 680RD EGF), 780 nm excitation (targeting IRDye® 800CW 2-DG), and mixed 665 nm-780 nm excitation (targeting both IRDye® 680RD EGF and IRDye® 800CW 2-DG).

Using the near-infrared information from our imaging system, each tissue sample was scored and classified as either tumor tissue or healthy tissue, and these predictions were compared against ground truth. The results of this analysis are detailed in the receiver operating characteristic (ROC) curves shown in Fig. 4a, where an area under the curve (AUC) of 0.92 can be observed under mixed 665 nm-780 nm excitation (IRDye® 680RD EGF and IRDye® 800CW 2-DG together) compared to 0.77 for 665 nm excitation (IRDye® 680RD EGF alone) and 0.75 for 780 nm excitation (IRDye® 800CW 2-DG alone). Accounting for the paired design of the imaging study, a dual-tracer strategy using EGF and 2-DG together significantly outperforms single-tracer use of EGF ($p = 0.022$) and single-tracer use of 2-DG ($p = 0.016$) when comparing AUCs. Considering the difference between the AUC for the EGF/2-DG scenario and the AUCs for the single-tracer scenarios, the 95% confidence interval was

indeed (0.03–0.29) for the EGF scenario and (0.04–0.36) for the 2-DG scenario, indicating a statistically significant improvement in tumor scoring.

All three visible channels are required for color imaging of the surgical site, while two near-infrared channels are required for near-infrared imaging of the fluorescent dyes (IRDye® 680RD EGF with $\lambda_{em} \approx 693$ nm and IRDye® 800CW 2-DG with $\lambda_{em} \approx 780$ nm)—accounting for five of the image sensor's spectral channels. The third near-infrared channel is dedicated to three-dimensional reconstruction using structured illumination from a near-infrared projector (at $\lambda \approx 900$ nm), ensuring full use of all six channels. The projector illuminates the surgical site with a sinusoidal pattern advancing along the wavefront normal, while an algorithm compares the observed phase change to the expected phase change and extracts the phase change induced by the three-dimensional topography; an inverse model then facilitates conversion of these phase changes into a height map. These three-dimensional reconstructions can be generated at a spatial resolution of 1280 by 720 pixels and a frame rate of 30 frames per second while exhibiting an average root-mean-square error of 1.179 mm and an average signal-to-noise ratio of 36.

Representative images of a mouse before surgery showing both the fluorescently labeled tumors and the three-dimensional reconstruction are provided in Fig. 4b; an animation of these images is provided in Supplementary Video S1. Three visible channels worth of information are used to visualize the mouse, while two near-infrared channels worth of information are used to detect the tumors (Fig. 4c); the remaining near-infrared channel worth of information is used to extract the shape of the mouse and the tumors within the mouse (Fig. 4d). In this figure, the tumors are highlighted in either green or blue to emphasize preferential accumulation of either IRDye® 680RD EGF or IRDye® 800CW 2-DG as measured by tumor-to-background ratios under 665 nm excitation and 780 nm excitation, emphasizing that different tumors may be more easily detected with different dyes; in the operating room, however, the tumors would normally be identified together under mixed 665 nm-780 nm illumination, permitting the greater diagnostic performance demonstrated by the ROC analysis. This diagnostic information, coupled with inherently co-registered shape information, improves tumor detection despite intertumoral variation and indicates the tumor's size/extent, offering additional information to optimize surgical resection.

Clinical Feasibility of Sentinel Lymph Node Detection for Patients with Breast Cancer

To explore the translation of the multifluorophore surgical workflow proved in small-animal models to a clinical environment, our imaging system was used to visualize fluorescently labeled sentinel lymph nodes in patients with early-stage breast cancer. In conventional surgical practice, sentinel lymph node mapping involves the peritumoral administration of radioactive tracers like Tc-99m sulfur colloid that can be identified with a gamma probe and dark-colored dyes like ICG and MB that can be observed with the naked eye. Since ICG and MB are both near-infrared fluorophores, though, it is possible to detect these dyes by their near-infrared fluorescence, enabling identification of sentinel lymph nodes without the radioactivity associated with radiotracers and the limited depth of visualization associated with visible stains. According to the standard of care, Tc-99m sulfur colloid, MB, and ICG were administered prior to breast cancer surgery. Based on radioactive signals and visual cues, all suspected lymph nodes were removed from the patient and imaged with our imaging system under 780 nm excitation (for ICG detection), 665 nm excitation (for MB detection), and mixed 780 nm-665 nm excitation (for dual ICG-MB detection). Immediately thereafter, the suspected lymph nodes underwent histopathologic analysis to determine whether the resected tissues were lymphatic structures and to evaluate whether they exhibited metastases.

Representative images of sentinel lymph nodes *in vivo* during and *ex vivo* after surgery are provided in Fig. 5b-f; a video from our imaging system in the operating room is provided in Supplementary Video S2, and a picture of our imaging system in the operating room is provided in Fig. 5a. *In vivo*, ICG and MB collect in different regions of the surgical site at different moments during the operation (Fig. 5b-d). From the injection of the dyes through the massage of the tissues to the beginning of resection, the dyes migrate from the injection site to the lymph node as scalpels, retractors, and other tools are introduced throughout the nonstop procedure; in such a dynamic environment where fluorophores may be uncovered or covered, modulating the fluorescent emission, and where tools are constantly moving, absorbing or reflecting the fluorescent excitation, it is critical that relevant fluorescent emission be detected and that irrelevant fluorescent excitation be rejected—all under surgical illumination. Our imaging system, which is capable of detecting weak fluorescence emission and differentiating between fluorescence emission and excitation, was able to identify lymph nodes under such demands. *Ex vivo*, ICG and MB concentrate at different points in different lymph nodes (Fig. 5e,f). As the dyes travel through the lymphatic basin into a lymph node, they may exhibit differences in accumulation based on disparities in molecular weight, hydrodynamic radius, or charge; such variation may arise to the point that one dye exhibits a homogeneous response and another dye a highly heterogeneous response even though both dyes were injected in a similar time and place. Again, our imaging system, which is capable of spectrally differentiating the dyes and using this spectral information in application, was able to identify lymph nodes in such a context.

Ultimately, our imaging system succeeds at detecting sentinel lymph nodes, providing an AUC of 88% (95% confidence interval: 77.9–96.6%) on *ex vivo* samples with ICG as well as a true positive rate of 84% (95% confidence interval: 73.5%–93.9%) and a false positive rate of 0% (95% confidence interval: 0–0%) at maximal Youden's index. However, further investigation into paired dye detection is required before clinical adoption for detecting sentinel lymph nodes. ICG and MB accumulate in lymph nodes via the same mechanisms, suggesting that they should accumulate in the same lymph nodes, but the two dyes exhibit differences in physiochemical properties that manifest as differences in where they accumulate within those lymph nodes; larger studies are needed to understand these differences in accumulation and examine whether they have an impact on diagnostic performance.

Discussion

When successfully translated to the medical field, new sensing technologies can decrease patients' medical expenses, increasing their quality of life, and directly impact our economy and society. In most hospitals, the primary sensing modalities during surgical procedures are the surgeon's eyesight and touch, leading to subjective discrimination between cancerous and healthy tissues; therefore, there has been intense interest in and numerous proposals for imaging systems that can eliminate the positive tumor margins associated with tumor regrowth and the overly negative tumor margins associated with iatrogenic effects. Unfortunately, imaging technologies have faced little success being adopted into the operating room; the imaging architectures that have come to dominate within the last 50 years of semiconductor and optical research have produced biomedical imaging systems that are incompatible with the clinical environment and lack diagnostic performance.

In this work, we have presented a bio-inspired image sensor with hexachromatic vision for image-guided surgical applications. The sensor, which is realized by monolithically integrating an array of vertically stacked photodetectors with an array of pixelated spectral filters, enables the differentiation of multiple fluorophores across a surgical site and in real time, providing physicians with the critical information required to make surgery-time decisions and enhance surgical outcomes. Near-infrared images are inherently co-registered with visible images in both time and space, eliminating the

ambiguity between anatomical features and fluorescently labeled structures that can turn a perfect incision into a poor prognosis. Tumor detection in preclinical models of human prostate cancer indicate that this technology can improve the accuracy of resection as tumor-targeted markers enter clinical practice, while sentinel lymph node detection in clinical management of breast cancer suggests that this technology can already play a role, providing surgeons with the spectral information that can isolate fluorescence emission from excitation and elucidate fluorescence heterogeneity. With these imaging capabilities, plus a compact footprint and low weight that can be seamlessly integrated into space-constrained operating rooms, our bio-inspired imager can open unprecedented opportunities for quality-based health care in both resource-limited and resource-rich hospitals.

Materials and Methods

Assembly and Operation of Imaging System

The array of three vertically stacked photodiodes was fabricated using a specialized 180 nm CMOS process and packaged in a ceramic housing by Sigma Corporation, and the array of pixelated long-pass filters and short-pass filters was produced using alternating steps of deposition and lift-off on a glass substrate by Salvo Technologies. The imager and filters were aligned using a submicron-resolution, six-degree-of-freedom positioning stage and were flip-chip bonded using ultraviolet-curing optical adhesives at the University of Illinois at Urbana-Champaign.

As appropriate, several transformations were applied to images captured with the system according to accepted practice in the imaging community. To account for dark currents and other offsets, dark images were removed from images before additional processing. To mitigate the effects of spatial nonuniformity in the image sensor, an affine transformation was applied across all photodiodes and all channels so that every photodiode in each channel would return an identical value when illuminated by a uniform source. To bring the spectral response provided by the image sensor in line with the spectral response provided by the human eye, an affine transformation was applied to convert the three measurements made at every pixel in the color channel to the color measurements that would be made at every pixel by a CIE 1931 standard observer.

Optoelectronic Characterization

The transmissions and optical densities of the spectral filters were reported by the manufacturer and are reproduced here.

To evaluate the image sensor's normalized quantum efficiencies, an integrating sphere (IS200-4, Thorlabs) was used to couple light from a computer-controlled monochromator (Acton SP2150 w/ TS-428 bulb, Princeton Instruments) to either the image sensor under test or a power meter (PM100D w/ S120VC sensor, Thorlabs). The monochromator was programmed to sweep from 400 nm to 1000 nm in 5-nm steps, and the image sensor and power meter were used to collect a video and measure the irradiance at each step. First, a responsivity curve was produced for each channel. The videos were temporally averaged (over 10 frames) and spatially trim-averaged (over all pixels, removing 2.5% from each extreme), providing a per-pixel digital number for each channel, while the irradiances were multiplied by the pixel's fill factor, photosensitive area, and integration time and divided by the appropriate photon energy, providing a per-pixel photon count; the responsivity curve for each channel was produced by dividing the per-pixel digital numbers for that channel by the per-pixel photon counts. Second, a normalized quantum efficiency curve was produced for each channel. A normalization factor was computed for each channel (defined by a layer of photodiodes and a type of filter) by taking the maximum value across the responsivity curves associated with that layer of photodiodes and both types

of filters; the normalized quantum efficiency curve for each channel was computed by dividing the responsivity curve for that channel by the normalization factor for that channel.

To evaluate the image sensor's read noise and dark current, a lens cap was installed over the image sensor under test. The image sensor was used to collect videos at multiple integration times. To compute the read noise, the temporal standard deviation was computed over each video (over 100 frames), the spatial average was computed over the temporal standard deviations (over all pixels), and a plot was produced of spatially averaged temporal standard deviation versus integration time; a linear function was fitted to the data, and the read noise was taken as the spatially averaged temporal standard deviation extrapolated to minimum integration time. To compute the dark current, the spatiotemporal average was computed over each video (over 100 frames and all pixels), and a plot was produced of spatiotemporal averages versus integration time; a linear function was fitted to the data, and the dark current was taken as the slope.

To evaluate the image sensor's full-scale range, an integrating sphere (819D-IS-5.3, Newport) was used to couple light from color LEDs (LZ4-00R108, LZ4-00G108, and LZ4-00B208, LED Engin) to the image sensor under test. Since identical photodiodes were used under the short-pass filters and the long-pass filters, the full-scale range for the photodiodes were measured under the short-pass filters and assumed equal under the long-pass filters; accordingly, the bottom photodiodes were probed with the red LED, the middle photodiodes were probed with the green LED, and the top photodiodes were probed with the blue LED. Current was switched between the LEDs as the integration time was adjusted on the image sensor, providing videos for each LED at multiple integration times. The videos were spatiotemporally averaged at each integration time (over all pixels and 100 frames), and a plot was produced of spatiotemporal average versus integration time; a piecewise function composed of a linear function (modeling the linearity of the image sensor) and an inverse exponential function (modeling the saturation of the image sensor) was fitted to the data. The bottom of the full-scale range was found by extrapolating the piecewise function's linear portion to shorter integration times and finding the digital value at zero integration time, while the top of the full-scale range was found by extrapolating the piecewise function's linear portion to larger integration times and finding the digital value where the percent residual between the extrapolated line and actual data exceeded ±1% for the last time; the full-scale range was defined as the difference between these two digital numbers.

To evaluate the image sensor's fixed pattern noise, an integrating sphere (819D-SF-4 or 819D-IS-5.3, Newport) was used to couple light from an incandescent lamp (OSL1 w/ OSL1B bulb, Thorlabs) to the image sensor under test. The incandescent lamp generally induced a larger response under the long-pass filter than under the short-pass filter and in the deeper photodiodes than in the shallower photodiodes, so smaller currents/shorter integration times were generally used for those channels that were more responsive than for those channels that were less responsive. Current was driven into the incandescent lamp as the integration time was adjusted on the image sensor, providing videos for each current at multiple integration times. The video was identified where the spatiotemporal average fell closest to half the full-scale range; this video was temporally averaged (over 100 frames), spatially cropped (to 95% of the frame), and both subtracted by the spatial mean (providing an array of deviations from the mean) and divided by the spatial mean (providing an array of percent deviations from the mean). A histogram was produced over the array (producing the fixed pattern noise histogram), and the standard deviation was computed over the histogram (producing the fixed pattern noise).

Fluorescence Sensitivity

For the experiments in this section, the image sensor was equipped with a photographic lens (50mm f/1.4 AS IF UMC, Rokinon, or EF 50 mm f/1.2L USM, Canon), and samples were kept in 1.5-mL microcentrifuge tubes (022363204, Eppendorf). Unless otherwise noted, a diode laser (BWF2-780, B&W Tek), a laser-shaping filter (FF01-769/41 Brightline bandpass filter, Semrock), and a diffusing lens (ACL2520U-DG15, Thorlabs) were used to produce 780 nm illumination, while another diode laser (BWF2-665, B&W Tek), a laser-shaping filter (665.85-1 OD6 Ultra Narrow Bandpass Filter, Alluxa), and a diffusing lens (ACL2520U-DG15, Thorlabs) were used to produce 665 nm illumination.

To determine the detection limit for indocyanine green (ICG) in fetal bovine serum (FBS), solutions of ICG in 90% FBS were produced via half-log dilution from 1 μM to 100 pM and log dilution from 100 pM to 1 pM. Control samples of FBS were collected both before and after serial dilution (2 total FBS samples), and experimental samples of ICG in FBS were collected at each concentration (11 total ICG/FBS samples). The lens (Rokinon) was adjusted to f/2.0 aperture, the sensor was configured with 200-ms exposure time, and the 780 nm illumination was tuned to 20 mW/cm^2. Control samples were imaged at the beginning and end of the study, with all experimental samples between. In this work, the limit of detection was taken as the concentration of fluorophore where the average fluorescent signal exceeded the read noise 99.86% of the time at 50% of the pixels. For each experimental sample as well as the control samples, videos were converted from a red-green-blue representation to a hue-saturation-value representation; the intensity information encoded in the value was retained, while the spectral information encoded in the hue and saturation were discarded. For each experimental sample, the signal at each pixel was established by taking the temporal mean at each pixel (over 25 frames), and for the control samples, the noise floor at each pixel was established by summing the temporal mean at each pixel and three times the temporal standard deviation at each pixel (over 25 frames and averaged across vials). Given an experimental sample, a detection was registered (at 1769 pixels near the vial centers) where the signal exceeded the noise floor, and the detection rate was determined by dividing the number of detections by the number of pixels. For experimental samples where the detection rate exceeded 0.5, the signal was considered correctly detected, with the signal otherwise considered incorrectly missed; the detection limit was taken as the experimental sample with the smallest concentration yielding a detection rate $\geq$0.5.

To demonstrate the capability to differentiate ICG dissolved in two different media, solutions of ICG in deionized water and in FBS were produced at a concentration of 3 μM. One sample of each solution was collected. The lens (Canon) was adjusted to f/2.2 aperture, the sensor was configured with 200-ms exposure time, and the 780 nm illumination was tuned to 25 mW/cm^2. Videos were captured of each sample and converted from a red-green-blue representation to a hue-saturation-value representation; the spectral information encoded in the hue and saturation was retained, while the intensity information encoded in the value was discarded. For each solvent, a collection of hue-saturation points was produced by this process; a region of interest of 30-by-30 pixels across 30 frames (27,000 total pixels) was selected, and a 95% tolerance ellipse was obtained using the procedures described in the Statistical Analysis subsection below. The hue-saturation points and the tolerance ellipses were plotted to reveal differentiability between the two solutions. To demonstrate the capability to differentiate between different ratios of IRDye® 680RD and IRDye® 800CW, solutions of IRDye® 680RD and IRDye® 800CW in phosphate-buffered saline were produced at a concentration of 1 μM, and mixtures of the stock solutions were made at volumetric ratios of 10:0, 9:1, 7:3, 5:5, 3:7, 1:9, and 0:10. One sample of each mixture was collected. The lens (Canon) was adjusted to f/2.2 aperture, the sensor was configured with 200-ms exposure time, and the 780 nm and 665 nm illumination were each tuned to 20 mW/cm^2. Videos were captured of each sample and analyzed as previously described.

To demonstrate that excitation and emission spectra could be differentiated, a scene containing a mixture between excitation and emission spectra was assembled. The 780 nm illumination from a diode laser (BWF2-780, B&W Tek) was passed through a laser-shaping filter (FF01-769/41 Brightline bandpass filter, Semrock), a ground glass diffuser (DG05-120, Thorlabs), and a condenser lens (ACL25416U, Thorlabs) before incidence on a 50:50 beamsplitter (CM1-BS1, Thorlabs). One half of the total power was directed toward a condenser lens (ACL25416U, Thorlabs) and a ground glass diffuser (DG05-120, Thorlabs) such that this light could be projected outward; the other half was directed toward ICG in deionized water stored in a microcentrifuge tube such that the light could generate fluorescence emission within or reflect off the microcentrifuge tube. The lens (Rokinon) and sensor were set up such that they viewed the projected excitation from the first optical path as well as the fluorescence emission and reflected excitation from the second optical path. A 50-frame color/near-infrared video of the scene was captured, and the temporally averaged near-infrared frame was transformed from a red-green-blue representation to a hue-saturation-value representation. Pixels were selected from two regions of interest that corresponded to pure excitation signal (collected over the projection from the first optical path) and pure emission signal (collected from the center of the vial in the second optical path); pixels were discarded if the value was too close to the noise floor or too close to saturation. The value and its intensity information were trimmed away, while the hue and saturation and their spectral information were retained; a binary linear support vector machine capable of predicting pure excitation signal or pure emission signal was then trained on the hues and saturations. Recognizing that the mixed excitation-emission signal should lie between pure excitation signal and pure emission signal and that the binary linear support vector machine's margin should lie between these two classes, a three-class classifier was derived that predicted mixed excitation-emission within the margin and either pure excitation or pure emission outside the margin. Pixels were then selected from another region of interest covering the entirety of the projection from the first optical path and the entirety of the vial in the second optical path. The value and its intensity information were trimmed away, while the hue and saturation and their spectral information were retained; the three-class classifier was then tested on the hues and saturations, labeling each pixel as mixed excitation-emission, pure excitation, or pure emission. Finally, a scatterplot was generated over the hue-saturation space using the pixels used to train the classifier, and an image was produced marking the pixel-wise classification from the pixels used to test the classifier.

Cell Culture

For the animal procedures, prostate cancer cell lines PC3 and LNCaP were obtained from the American Type Culture Collection (ATCC) and used for experiments within 6 months of their receipt. Cell lines were commercially tested for pathogens, including mycoplasma, through the University of Illinois Department of Animal Resources and Charles River Research Animal Diagnostic Services. All cells were cultured under the recommended conditions in a 37 ˚C humidified incubator with 5% CO_2 atmosphere.

Animal Experiments

All animal experiments were performed under protocols approved by the University of Illinois Institutional Animal Care and Use Committee. The studies complied with all relevant ethical regulations. Nude athymic J:NU mice (Jackson Laboratory) were used for *in vivo* tumor imaging and *ex vivo* receiver operating characteristic analysis (ROC). PC3 and LNCaP cells were incubated, grown to 90% confluence, detached, suspended in Matrigel, and delivered via subcutaneous injection. The suspension consisted of 2×10^7 cells per 100 μL of 10% Matrigel, and the injection comprised of 50 μL of cell-Matrigel solution. For some mice, two subcutaneous injections of LNCaP cells on the left

flank and two subcutaneous injections of PC3 cells on the right flank were delivered. For the remaining mice, two subcutaneous injections of PC3 cells, one on each flank, were delivered. The mice were monitored daily for tumors and were imaged when tumors grew to ~1 cm diameter.

At 24 hours preimaging, the animals were anesthetized with 1-2% isoflurane, and their skin was prepared using an alcoholic iodine solution and opened during a jugular vein cut-down procedure. For each mouse, two fluorophores were injected in sequence: 200 µL of 0.1 nmol/1 µL IRDye® 800CW 2-DG labeled with 2-deoxy-D-glucose followed by 100 µL of 2 nmol/100 µL IRDye® 680RD EGF labeled with human recombinant epidermal growth factor. Using a surgical microscope for direct visualization, each fluorophore was administered using a 30-gauge insulin syringe needle inserted into the jugular vein. After injection, gentle pressure was applied to the injection site with a cotton-tip swab for approximately 30 seconds before the skin was closed with a sterile 6-0 Prolene suture. All procedures were done under aseptic conditions.

At imaging time, the mice were anesthetized under 1-2% isoflurane on a heated bed; in vivo images were captured; the surgeon euthanized the mice and removed tissue samples, marking each as either cancer-positive tumor or cancer-negative muscle; and ex vivo images were captured. To mimic the case where IRDye® 800CW 2-DG alone was administered, ~20 mW⁄cm^2 intensity of 780 nm excitation was provided; to mimic the case where IRDye® 680RD EGF alone was administered, ~20 mW⁄cm^2 intensity of 665 nm excitation was provided; and to observe both IRDye® 800CW 2-DG and IRDye® 680RD EGF, both excitations were provided. The imaging system and excitation sources were set up at a ~0.5-m working distance. The image sensor was equipped with a Canon EF 50mm f/1.2 lens that was focused on the sample and adjusted to an aperture between ~f/2.0 and ~f/4.0. The imaging system was configured to provide a ~200-ms to ~400-ms exposure for the near-infrared pixels to ensure high signal-to-noise ratio in the fluorescence signal. A total of 7 mice were involved, and a total of 48 tissue samples were collected; these tissue samples included 24 tumor tissues (14 PC3 and 10 LNCaP) and 24 healthy tissues.

A multistep procedure was required to locate the tissue sample, extract the near-infrared features, and distinguish the tumor tissues from healthy tissues. Raw images were demosaiced and temporally averaged, and regions of interest corresponding to the tissue samples were selected by hand; these regions were spatially averaged. Near-infrared channels were then mapped from red-green-blue representations to hue-saturation-value representations; ultimately, the value (intensity information) was dropped during the classification procedure because the hue and saturation (spectral information) provided sufficient information about the tissue samples. Generation and analysis of ROC curves then followed the procedures described in the Statistical Analysis subsection below.

Three-Dimensional Reconstruction

To permit three-dimensional surface reconstruction, structured illumination was used. A near-infrared projector with a 900 nm lamp (EKB Technologies Ltd., Israel) and our imaging system with 900 nm sensitivity were synchronized such that a sinusoidal pattern could be projected onto an object by the near-infrared projector and captured at a high rate by our imaging system. After each frame, the projected pattern underwent a known phase shift, causing the captured pattern to experience an unknown phase shift associated with the object's topology; after 6 frames, a least-squares algorithm provided wrapped values for the unknown phase shift (*25*), and Goldstein's branch cut method provided unwrapped values for the unknown phase shift (*26*). Plugging in the phase shift at every pixel coordinate, a 12-term rational function provided the height at every pixel coordinate (*27*).

To facilitate calibration of the reconstruction model (i.e., the unknown coefficients in the 12-term rational function) and evaluation of the reconstruction error (i.e., between the predicted height and the actual height) a gauge object with known topology was utilized. The gauge object was designed with six ramps leading to six ledges and was fabricated in plastic via stereolithography (with tolerances of ±0.140 mm). Three ledges (at heights of 9.525 mm, 28.575 mm, and 41.275 mm) were designated for calibration of the reconstruction model, and three ledges (at heights of 15.875 mm, 22.225 mm, and 34.925 mm) were designated for evaluation of the reconstruction error. Sinusoidal fringes were projected onto the gauge object (with a period of ~14.50 mm along the ground plane) and were shifted across the gauge object (in discrete steps of 2.42 mm along the ground plane) as near-infrared images were captured (with ~5.78 pixels spanning 1 mm along the ground plane). The observed deformation of the sinusoidal fringes along the ramps and the known heights of the ledges were used to populate the reconstruction model via the Levenberg-Marquardt algorithm and to calculate the reconstruction error using the fitted model. The root-mean-square error and signal-to-noise ratio over multiple measurements was evaluated at each point on each evaluation step and was spatially averaged across each step and across all evaluation steps.

Human Study

All human studies were performed under protocols approved by the Institutional Review Board at the University of Illinois at Urbana-Champaign and the Agency for Drugs and Medical Instruments in Skopje, Republic of North Macedonia. The studies complied with all ethical regulations, and all procedures were executed in accordance with approved guidelines. Inclusion criteria for patients included: early or progressive stage of breast cancer and ability to understand and willingness to sign written informed consent documents. Exclusion criteria included: presence of inflammatory cancerous tissue, history of allergic reactions to iodide or seafood, failure to detect sentinel lymph nodes with radiocolloid and static gamma camera, history of breast surgery, pregnancy, and unwillingness to enter study. All patients gave informed consent for this HIPAA-compliant study. The study was registered on clinicaltrials.gov (trial ID no. NCT03619967).

Before the surgical procedure, Tc-99m sulfur colloid (834 μCi), ICG (2 mL at 0.5 mg ICG per mL saline), and methylene blue (MB;1 mL at 10 mg MB per mL water) were injected into the patient's tumor area, followed by 5 min of site massage; at 10–15 min postinjection, the surgeon proceeded with the surgery per standard of care. When suspected sentinel lymph nodes were identified using the radioactivity measured with a gamma probe and the visible contrast provided by MB and ICG, the tissues were removed. All resected samples were analyzed using histopathology to confirm or disaffirm sentinel lymph node status.

For one set of patients (7 patients; mean ± standard deviation age: 58 ± 12 years), images of tissues before and during resection were captured. Under operating conditions, bright light from broadband surgical lamps, ~10 mW/cm^2 from a 780 nm laser, and ~10 mW/cm^2 from a 665 nm laser were provided. The image sensor was configured to provide a 25-ms exposure for color pixels and a ~100- to ~200-ms exposure for near-infrared pixels and was equipped with a Canon EF 50mm f/1.2 lens adjusted to an aperture of ~f/2.2. The imaging system and excitation sources were set up at a ~2-m working distance. These *in vivo* samples were not incorporated into the ROC analysis. For the remaining patients (11 patients; mean ± standard deviation age: 61 ± 15 years), images of tissues after resection were captured. To mimic the case where ICG alone was administered, ~5 mW/cm^2 intensity of 780 nm excitation was provided; to mimic the case where MB alone was administered, ~5 mW/cm^2 intensity of 665 nm excitation was provided; and to observe both the ICG and MB, both excitations were provided. The image sensor was configured to provide a ~200-ms exposure for near-infrared

pixels and was equipped with a Rokinon 50mm f/1.4 lens adjusted to an aperture of ~f/2.0. The imaging system and excitation sources were set up at a ~0.5-m working distance. These *ex vivo* samples were incorporated into the ROC analysis: 55 tissue samples were collected of which 49 were lymph nodes and 6 were nonlymphatic structures.

A multistep procedure was required to locate the tissue sample, extract the near-infrared features, and distinguish the sentinel lymph nodes from nonlymphatic structures. Raw images were demosaiced and temporally averaged, and regions of interests corresponding to the tissue samples were selected by isolating a rectangular window at the image's center and extracting the largest contiguous region with average near-infrared response in the 95th percentile and above; these regions were spatially averaged. Near-infrared channels were then mapped from red-green-blue representations to hue-saturation-value representations. Generation and analysis of ROC curves then followed the procedures described in the Statistical Analysis subsection below.

Statistical Analysis

Generation of 95% tolerance ellipses in the fluorescence sensitivity studies followed existing procedures. Data points are defined as tuples of hues and saturations that lie in a polar coordinate system (i.e., where the hue is the angular coordinate and the saturation is the radial coordinate); however, data points are confined to a small enough region such that the tuples of hues and saturations can be taken to lie in a rectangular coordinate system (i.e., where the hue is the x-coordinate and the saturation is the y-coordinate). All data points were assumed drawn from a binormal distribution. A 95% tolerance ellipse is taken as an ellipse generated by a method has an approximately 95% probability of covering at least 95% of the population when the empirical mean and covariance are taken as sample estimators of the population statistics. As a result, the 95% tolerance ellipse can be computed using equation (5.9) reported in (*28*).

Generation of ROC curves in the animal study and human study followed similar procedures. To map the near-infrared signal in the hue-saturation-like/hue-saturation-value-like color space to a classification score appropriate for an ROC analysis without making assumptions on class covariance, quadratic discriminant analysis was used to model probabilities of class membership; to mitigate the risk of overfitting, stratified cross-validation was used in which the data set was broken into folds with equal class distributions and in which the discriminator was trained on out-of-fold samples and tested on in-fold samples. Conventional algorithms for ROC analysis could then be applied to the cross-validated probabilities to evaluate the area under the curve (AUC) for the scorer and to determine the optimal cut-point for a classifier.

Statistical analysis of ROC curves was facilitated using a resampling scheme based on the bootstrap method. A family of ROC curves was produced by generating stratified bootstrap samples of the tissue samples and generating ROC curves for each bootstrap sample. Confidence intervals for the AUCs, the true positive rates, and the false positive rates were computed using the bias-corrected and accelerated bootstrap interval: a bias-correction parameter related to statistical bias and an acceleration parameter related to statistical skewness were estimated from the data set and used to correct confidence intervals computed from bootstrapped samples. Confidence intervals were generated at 95% confidence.

Comparison of AUCs was facilitated using a bootstrap-based paired difference test. For each scenario of dye administration, stratified bootstrap samples were generated with the same tissue samples, and ROC curves and AUCs were computed for each bootstrap sample. To compare any two dye administration scenarios, the difference between the AUCs observed over all tissue samples was

computed, and the probability under the null hypothesis of the observed difference or a more extreme difference was found by finding the corresponding percentile in the distribution of differences between the paired AUCs observed for the bootstrap samples. These tests were run as one-tailed tests of superiority where, for example, the two-dye administration scenario could be presumed better than the one-dye administration scenario. All tests were run at a significance level of $\alpha = 0.05$.

References and Notes

1. L. V. Wang, J. Yao, A practical guide to photoacoustic tomography in the life sciences. *Nature Methods* **13**, 627-638 (2016).
2. H. Tu *et al.*, Stain-free histopathology by programmable supercontinuum pulses. *Nature Photonics* **10**, 534-540 (2016).
3. A. L. Vahrmeijer, M. Hutteman, J. R. van der Vorst, C. J. H. van de Velde, J. V. Frangioni, Image-guided cancer surgery using near-infrared fluorescence. *Nature Reviews Clinical Oncology* **10**, 507-518 (2013).
4. S. H. Yun, S. J. J. Kwok, Light in diagnosis, therapy and surgery. *Nature Biomedical Engineering* **1**, (2017).
5. R. Daw, J. Finkelstein, Lab on a chip. *Nature* **442**, 367 (2006).
6. G. Hong, A. L. Antaris, H. Dai, Near-infrared fluorophores for biomedical imaging. *Nature Biomedical Engineering* **1**, (2017).
7. G. M. van Dam *et al.*, Intraoperative tumor-specific fluorescence imaging in ovarian cancer by folate receptor-α targeting: first in-human results. *Nature Medicine* **17**, 1315-1319 (2011).
8. A. V. DSouza, H. Lin, E. R. Henderson, K. S. Samkoe, B. W. Pogue, Review of fluorescence guided surgery systems: identification of key performance capabilities beyond indocyanine green imaging. *BIOMEDO* **21**, (2016).
9. M. Garcia *et al.*, Bio-inspired imager improves sensitivity in near-infrared fluorescence image-guided surgery. *Optica* **5**, 413-422 (2018).
10. R. L. Siegel, K. D. Miller, A. Jemal, Cancer statistics, 2017. *CA: A Cancer Journal for Clinicians* **67**, 7-30 (2017).
11. E. R. Fossum, CMOS image sensors: electronic camera-on-a-chip. *IEEE Transactions on Electron Devices* **44**, 1689-1698 (1997).
12. C. Darwin, *On the origin of species by means of natural selection, or, The preservation of favoured races in the struggle for life*. (John Murray, London, England, 1859).
13. Y. M. Song *et al.*, Digital cameras with designs inspired by the arthropod eye. *Nature* **497**, 95-99 (2013).
14. H. H. Thoen, M. J. How, T.-H. Chiou, J. Marshall, A Different Form of Color Vision in Mantis Shrimp. *Science* **343**, 411-413 (2014).
15. T. W. Cronin, S. Johnsen, N. J. Marshall, E. J. Warrant, *Visual Ecology*. (Princeton University Press, Princeton, NJ, 2014).
16. J. A. Lenero-Bardallo, D. H. Bryn, P. Hafliger, Bio-Inspired Asynchronous Pixel Event Tricolor Vision Sensor. *IEEE Transactions on Biomedical Circuits and Systems* **8**, 345-357 (2014).
17. T. York *et al.*, Bioinspired Polarization Imaging Sensors: From Circuits and Optics to Signal Processing Algorithms and Biomedical Applications. *Proceedings of the IEEE* **102**, 1450-1469 (2014).
18. N. Niikura *et al.*, Loss of Human Epidermal Growth Factor Receptor 2 (HER2) Expression in Metastatic Sites of HER2-Overexpressing Primary Breast Tumors. *Journal of Clinical Oncology* **30**, 593-599 (2012).

19. N. J. Marshall, M. F. Land, C. A. King, T. W. Cronin, The compound eyes of mantis shrimps (Crustacea, Hoplocarida, Stomatopoda). I. Compound eye structure: the detection of polarized light. *Philosophical Transactions of the Royal Society B* **334**, 33-56 (1991).
20. Teledyne QImaging, "MicroPublisher 6™ CCD Camera Datasheet," (2019).
21. H. E. Rhodes, H. Nozaki, S. Manabe, "US2009/0200580A1 - Image sensor and pixel including a deep photodetector," (Omnivision Technologies, Inc., United States, 2009).
22. T. Dai, H.-C. Tai, S. Manabe, H. Nozaki, H. E. Rhodes, "US8228411B2 - Circuit and photo sensor overlap for backside illumination image sensor," (Omnivision Technologies, Inc, United States, 2012).
23. International Electrotechnical Commission, "Medical electrical equipment - Part 2-41: Particular requirements for the safety of surgical luminaires and luminaires for diagnosis (IEC 60601-2-41:2000)," (2000).
24. International Electrotechnical Commission, "Safety of laser products - Part 1: Equipment classification, requirements and user's guide (IEC 60825-1:1993+AMD1:1997+AMD2:2001 CSV)," (2001).
25. S. Zhang, S.-T. Yau, Generic nonsinusoidal phase error correction for three-dimensional shape measurement using a digital video projector. *Applied Optics* **46**, 36-43 (2007).
26. R. M. Goldstein, H. A. Zebker, C. L. Werner, Satellite radar interferometry: Two-dimensional phase unwrapping. *Radio Science* **23**, 713-720 (1988).
27. H. Du, Z. Wang, Three-dimensional shape measurement with an arbitrarily arranged fringe projection profilometry system. *Optics Letters* **32**, 2438-2440 (2007).
28. V. Chew, Confidence, Prediction, and Tolerance Regions for the Multivariate Normal Distribution. *Journal of the American Statistical Association* **61**, 605-617 (1966).
29. Z. Chen, X. Wang, R. Liang, RGB-NIR multispectral camera. *Optics Express* **22**, 4985-4994 (2014).
30. Z. Chen, N. Zhu, S. Pacheco, X. Wang, R. Liang, Single camera imaging system for color and near-infrared fluorescence image guided surgery. *Biomedical Optics Express* **5**, 2791-2797 (2014).

Acknowledgments: The authors thank James Hutchinson and Patricia J. Watson for manuscript editing. **Funding:** The work was funded by grants from the U.S. Air Force Office of Scientific Research (FA9550-18-1-0278), Congressionally Directed Medical Research Programs (W81XWH-19-1-0299), and National Science Foundation (2030421). **Author contributions:** V.G. conceived the idea behind the image sensor and oversaw the entire project. M.G. and V.G. designed the image sensor. Optical evaluation of the image sensor, including optoelectronic characterization and fluorescence sensitivity, was performed by S.B., M.G., T.D., and V.G. The cell culture was maintained by C.K. and L.W.D. Animal studies were designed, performed, and evaluated by S.B., M.G., T.D., C.K., K.K., L.W.D., S.N., and V.G. The three-dimensional reconstruction algorithm was developed and evaluated by S.B., M.G., and T.D. Human studies were designed, performed, and evaluated by S.B., M.G., T.D., R.C., I.F., B.K., S.S., M.B.T., N.T.D., N.J., D.M., G.P., G.K., and V.G. Statistical analysis was provided by S.B. and T.D. The manuscript was written by S.B., M.G., and V.G. All authors proofread the manuscript. **Competing interests:** The authors declare no competing interests. **Data and materials availability:** Requests for materials and other correspondence should be sent to Viktor Gruev at vgruev@illinois.edu.

Figures and Figure Captions

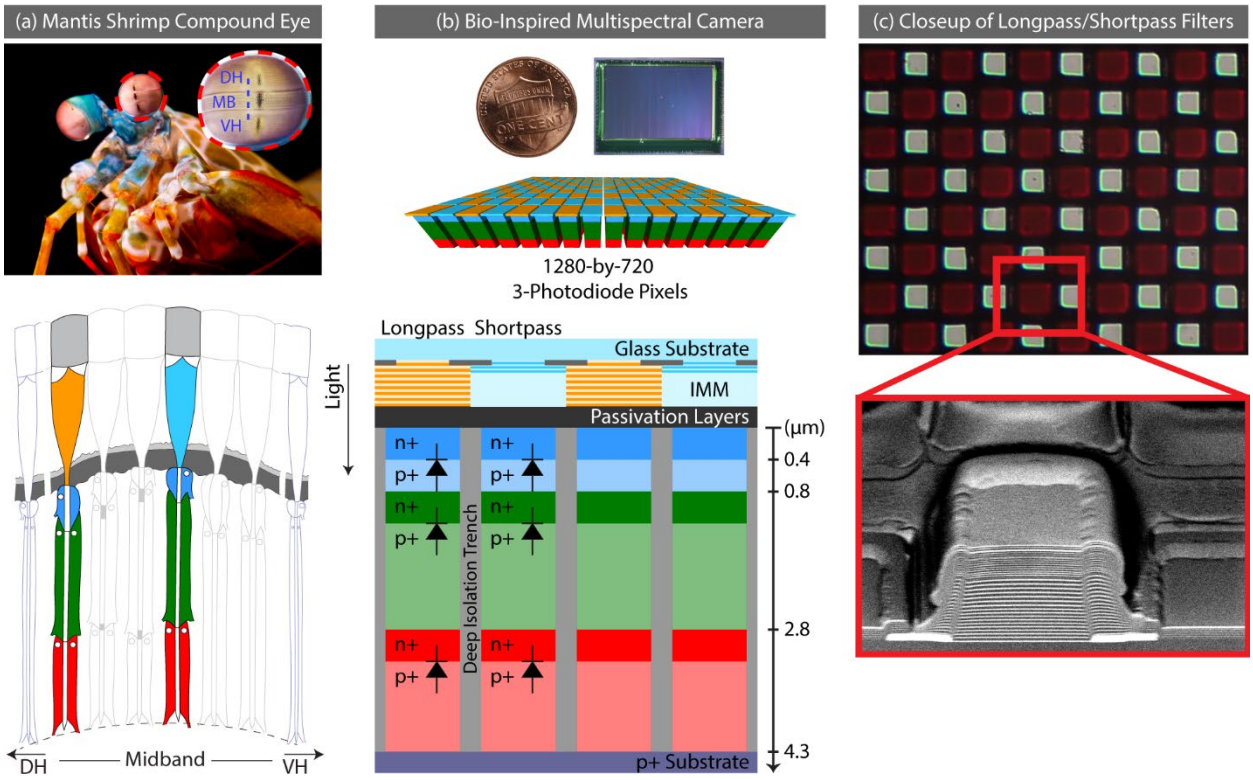

Fig. 1 | Diagrammatic comparison of the mantis shrimp compound eye and our bio-inspired image sensor. The midband section in the mantis shrimp uses a combination of vertically stacked photosensitive cells and spectral filters for spectral discrimination; reflective and absorptive pigments reduce optical crosstalk between neighboring rhabdomeres. Similarly, our image sensor uses a combination of vertically stacked photodetectors and interference filters to achieve simultaneous imaging of color and near-infrared light; isolation trenches between photodetectors and chromium lanes between filters reduce electrical/optical crosstalk between neighboring pixels. (a) Close-up views of the stomatopod *Odontodactylus scyllarus*'s compound eye (top) and a cross-sectional diagram showing the photosensitive cells and spectral filters (bottom). (b) Micrograph and diagrammatic representation of our imager (top) and a cross-sectional diagram showing the vertically stacked photodiodes and interference filters (bottom). (c) Optical microscope image of the pixelated optical filters (top) showing the long-pass filters in dark red and the short-pass filters in bright white, and a scanning electron microscope image of a long-pass filter in the center and short-pass filters on both sides (bottom). Abbreviations: dorsal hemisphere (DH), index-matching material (IMM), midband (MB), ventral hemisphere (VH).

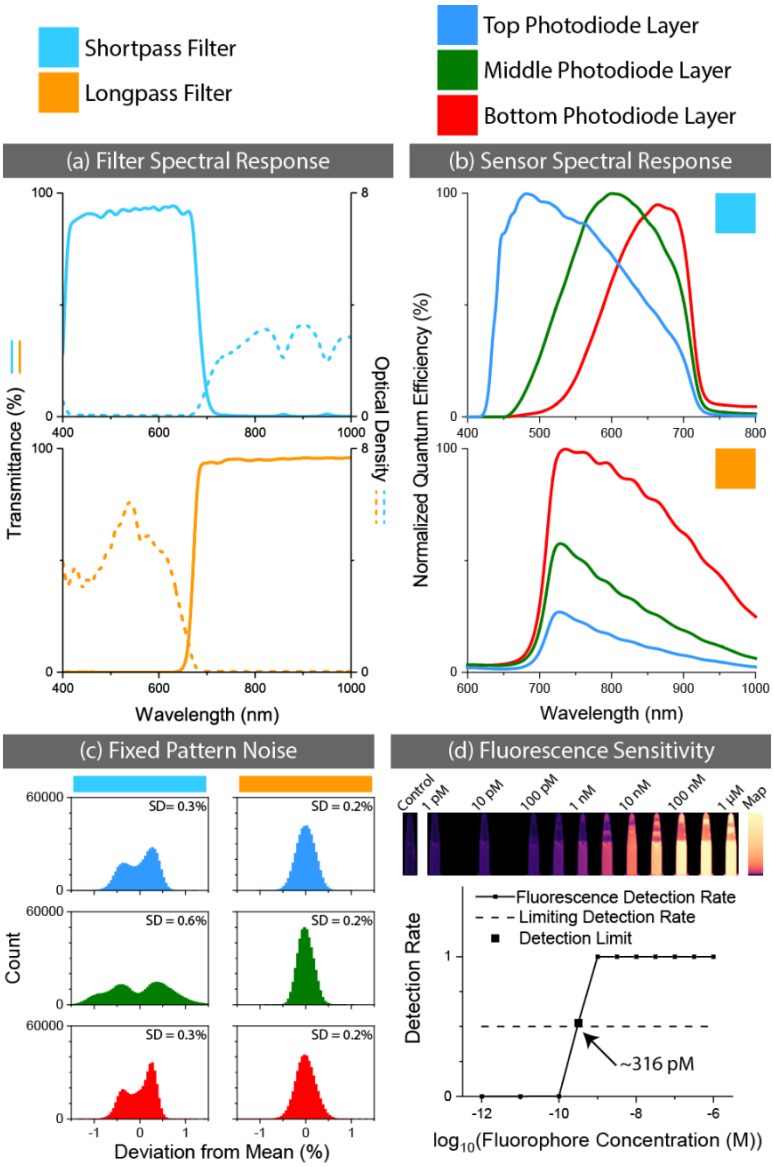

Fig. 2 | Optoelectronic characteristics of our bio-inspired imager. (a) Transmission and optical density curves for the short-pass filters (top) and long-pass filters (bottom). (b) Normalized quantum efficiency curves for the three photodiode layers under the short-pass filters (top) and long-pass filters (bottom). (c) Fixed pattern noise histograms at half full-scale range for the three photodiode layers under the short-pass filters (left) and long-pass filters (right). The fixed pattern noise is the standard deviations of the histograms. (d) Detection rate for different concentrations of indocyanine green. The detection limit is the minimum concentration (316 pM) with a detection rate above 0.5. Abbreviation: standard deviation (SD).

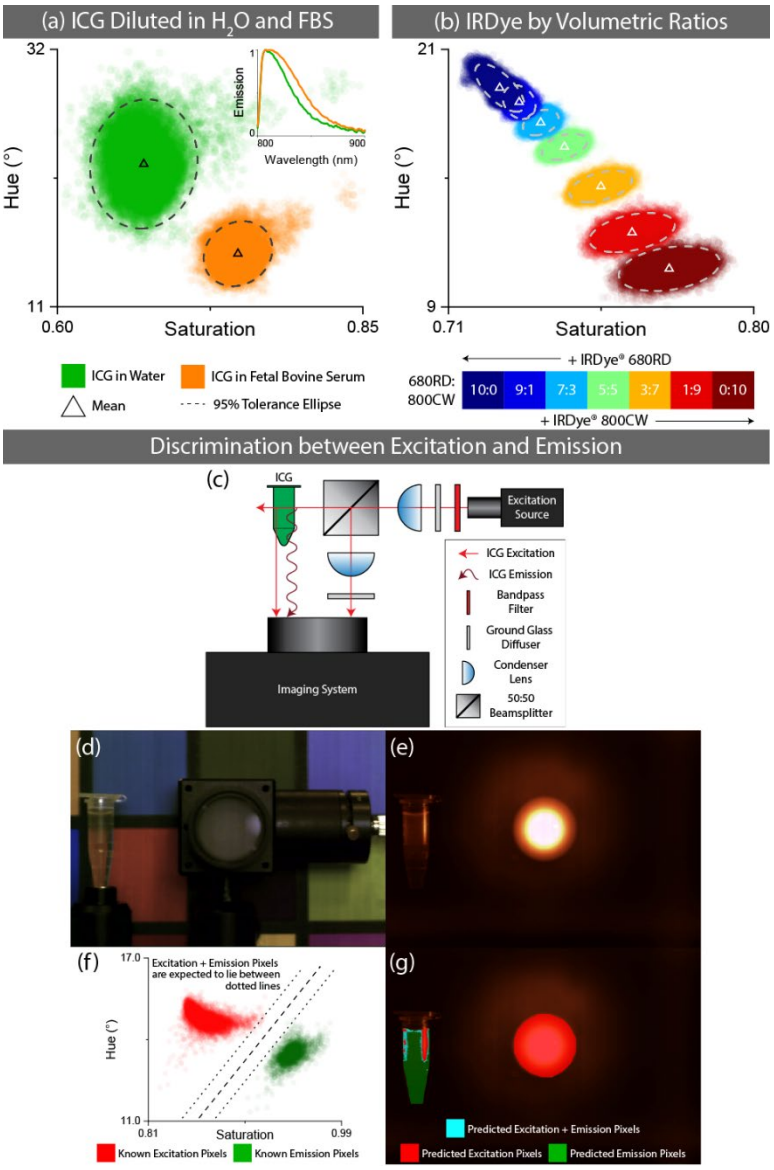

Fig. 3 | Imaging capabilities of our bio-inspired imager. (a) Discrimination of indocyanine green diluted in two different media—deionized water and fetal bovine serum—with both temporal and spatial noise. Observations of different solutions appear in different clusters in the main scatterplot. Emission spectra for the two solutions are inset in the top-right. (b) Discrimination of IRDye® 680RD and IRDye® 800CW mixed in different volumetric ratios with both temporal and spatial noise. Observations of different ratios appear in different clusters. (c-g) Discrimination of indocyanine green excitation and emission with spatial noise. (c) Experimental setup. (d) Color image of scene. Excitation is projected from the port; emission is generated in and excitation reflects from the vial. (e) Near-infrared image of scene. Pure excitation is observed inside the port; pure excitation, pure emission, and mixed excitation-emission are observed inside the vial. (f) Observations of pure excitation and pure emission cluster differently, permitting classification via a simple margin classifier such as a linear support vector machine. Observations of mixed excitation-emission should lie between and are classified accordingly. (g) Labels of pure excitation, pure emission, and mixed excitation-emission can be applied to the near-infrared image using the classifier. Abbreviation: indocyanine green (ICG).

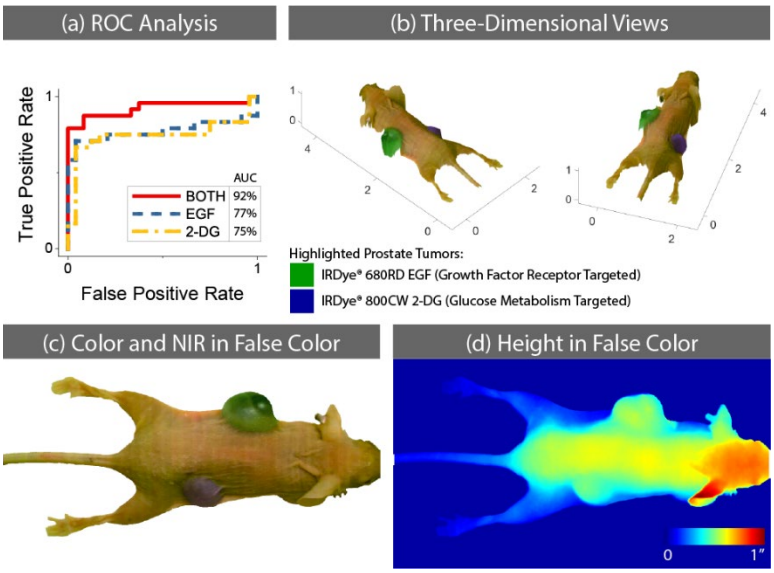

Fig. 4 | Animal study with our bio-inspired imaging sensor to detect tumors using IRDye® 680RD EGF and IRDye® 800CW 2-DG. (a) Receiver operating characteristic curves for tumor detection using both dyes together and each dye alone. Area under the curve improves for two dyes compared to one dye. (b) Two views of a mouse showing the estimated three-dimensional profile and the tumors highlighted with different targeted probes (see also Supplementary Movie S1). (c) Color/near-infrared image of a mouse showing the tumors highlighted with different targeted probes as indicated by tumor-to-background ratio. (d) Three-dimensional profile of a mouse indicating the out-of-plane height as extracted from structured illumination. Abbreviations: area under the curve (AUC), near-infrared (NIR), receiver operating characteristic (ROC).

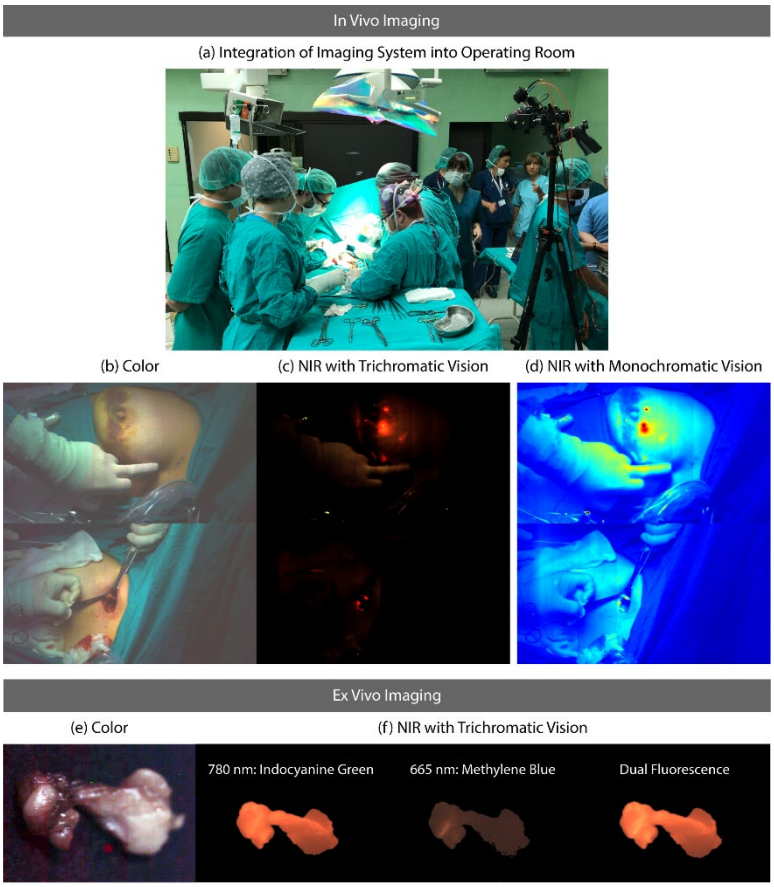

Fig. 5 | Clinical feasibility study with our bio-inspired imaging sensor to map sentinel lymph nodes using indocyanine green and methylene blue. (a) Integration of imaging system into operating room. (b-d) *In vivo* images before and after the incision for lymph node removal (see also Supplementary Movie S2). (b) Color images. (c) Near-infrared images in trichromatic format (i.e., with spectral discrimination). Injection points and sentinel lymph nodes exhibit high signal-to-background ratio with no false positives due to specular reflections. (d) Near-infrared images in monochromatic format (i.e., without spectral discrimination). Surgical instruments appear as false positives due to strong signal from specular reflection. (e, f) *Ex vivo* images of a resected lymph node. (e) Color image. (f) Near-infrared image representing indocyanine green alone (left), methylene blue alone (center), and both dyes together (right). Different dyes accumulate in different sites. Abbreviation: near-infrared (NIR).

SUPPLEMENTARY MATERIALS

Supplementary Fig. S1: Demonstration of our bio-inspired imaging system's color reproduction for natural scenes.

Supplementary Movie S1: Tumor detection in small-animal model of human prostate cancer showing overlaid information from color images of mouse, near-infrared images of fluorescently labeled tumors, and three-dimensional shape of mouse and tumors.

Supplementary Movie S2: Sentinel lymph node mapping in patients with breast cancer using near-infrared fluorescence from indocyanine green.

Supplementary Table S1: Optical performance of state-of-the-art near-infrared fluorescence (NIRF) imaging systems compared with our bio-inspired NIRF imager.

Supplementary Table S2: Optical performance of pixelated near-infrared fluorescence (NIRF) imaging systems compared with our bio-inspired NIRF imager.

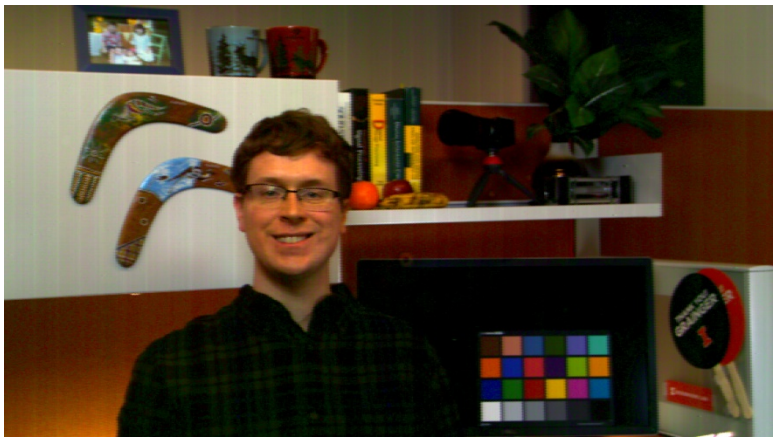

Supplementary Fig. S1 | Demonstration of our bio-inspired imaging system's color reproduction for natural scenes.

[Placeholder; See attached files.]

Supplementary Movie S1 | Tumor detection in small-animal model of human prostate cancer showing overlaid information from color images of mouse, near-infrared images of fluorescently labeled tumors, and three-dimensional shape of mouse and tumors.

[Placeholder; See attached files.]

Supplementary Movie S2 | Sentinel lymph node mapping in patients with breast cancer using near-infrared fluorescence from indocyanine green.

Supplementary Table S1 | Optical performance of state-of-the-art near-infrared fluorescence (NIRF) imaging systems compared with our bio-inspired NIRF imager.

Device	*Fluobeam 800*	*PDE Neo*	*SPY Elite*	*Iridium*	*Spectrum*	*Solaris*	*Bio-inspired*	*Bio-inspired*
Company or university	Fluoptics	Hamamatsu	Novadaq	VisionSense	Quest	PerkinElmer	Illinois & WUSTL	Illinois
Reference	(*8*)	(*8*)	(*8*)	(*8*)	(*8*)	(*8*)	(*9*)	This article
FDA/EMA approved	Yes	Yes	Yes	Yes	Yes	No	No	No
Instrument architecture	Single sensor	Single sensor w/ swappable filters	Single sensor	One–two sensors w/ dual optical paths	Three sensors w/ trichroic prism	Two sensors w/ beamsplitter	Single sensor	Single sensor
Sensor type	CCD	CCD	CCD	CCD	CCD	sCMOS	CMOS	CMOS
Permitted surgical lighting	Dim	Dim	Dim	Dim	On	On	On	On
Supports RGB imaging	No	Yes	No	Yes	Yes	Yes	Yes	Yes
Supports real-time RGB/NIR overlay	No	No	No	Yes	Yes	Yes	Yes	Yes
Number of NIR channels	1	1	1	1	2	2	1	3
Number of simultaneous NIR channels	1	1	1	1	2	1	1	3
Excitation source	750-nm laser	760-nm LEDs	805-nm laser	805-nm laser	LEDs	Filtered LEDs	780-nm laser	665- and 780-nm lasers
Fluorescence detection limit	~5 nM[a]	~15 nM[a]	~5 nM[a]	~50 pM[a]	~10 nM[a]	~1 nM[a]	100 pM[b]	316 pM[c]
Resolution (px)	720 x 576	640 x 480	1024 x 768	960 x 720	NS	1024 x 1024	1280 x 720	1280 x 720
Bit depth	8	8	8	12	12	16	14	14
Maximum frame rate (FPS)	25	NS	NS	NS	20	100	40	30

[a] IRDye® 800CW fluorescence marker was used for the experiment. Limit of detection was computed by plotting the average signal versus concentration and finding the intersection between the line fit to low concentrations and the line fit to high concentrations.
[b] Indocyanine green fluorescence marker was used for the experiment. Limit of detection was computed by modeling the average pixel's response to each concentration and finding the concentration where the average pixel fails to detect the concentration.
[c] Indocyanine green fluorescence marker was used for the experiment. Limit of detection was computed by modeling every pixel's response to each concentration and finding the concentration where most pixels fail to detect the concentration.

Abbreviations: CCD, charge-coupled device; CMOS, complementary metal-oxide semiconductor; EMA, European Medicines Administration; FDA, U.S. Food and Drug Administration; FPS, frames per second; Illinois, University of Illinois at Urbana-Champaign; NIR, near infrared; NS, not stated; RGB, red, green, blue; sCMOS, scientific complementary metal-oxide semiconductor; WUSTL, Washington University in St. Louis.

Supplementary Table S2 | Optical performance of pixelated near-infrared fluorescence (NIRF) imaging systems compared with our bio-inspired NIRF imager.

Device	*Piranha4*	*OV4682*	*RGB-NIR*	*Bio-inspired*	*Bio-inspired*
Company or university	Teledyne DALSA	OmniVision	Univ. of Arizona	Illinois & WUSTL	Illinois
Reference	Company website	Company website	(*29*), (*30*)	(*9*)	This article
Sensor type	Line scan CMOS	Full frame CMOS	Full frame CMOS	Full frame CMOS	Full frame CMOS
Filter material	NS	NS	Polymer	Dielectric interference filters	Dielectric interference filters
Supports multiple integration times	Yes	No	No	Yes	Yes
Supports RGB imaging	Yes	Yes	Yes	Yes	Yes
Number of NIR channels	1	1	1	1	3
Maximum OD of NIR filters in visible spectrum	NS	NS	NS	~2.5	~6.2
Maximum OD of RGB filters in NIR spectrum	NS	NS	NS	~2.1	~3.3
ICG detection limit	NS	NS	130 nM[a]	100 pM[a]	316 pM[b]
Resolution (px)	2048 x 4	2688 x 1520	2304 x 1296	1280 x 720	1280 x 720
Bit depth	12	10	12	14	14
Maximum frame rate (FPS)	NA	90	60	40	30

[a] Limit of detection was computed by modeling the average pixel's response to each concentration and finding the concentration where the average pixel fails to detect the concentration.
[b] Limit of detection was computed by modeling every pixel's response to each concentration and finding the concentration where most pixels fail to detect the concentration.

Abbreviations: CMOS, complementary metal-oxide semiconductor; FPS, frames per second; ICG, indocyanine green; Illinois, University of Illinois at Urbana-Champaign; NIR, near infrared; NA, not applicable; NS, not stated; OD, optical density; RGB, red, green, blue; WUSTL, Washington University in St. Louis.

A 120 dB Dynamic Range Logarithmic Multispectral Imager for Near-Infrared Fluorescence Image-Guided Surgery

Steven Blair[1], Nan Cui[2], Missael Garcia[1], and Viktor Gruev[1,3,*]
[1]Department of Electrical and Computer Engineering, University of Illinois at Urbana-Champaign, Urbana, IL, USA
[2]Department of Electrical and Systems Engineering, Washington University in St. Louis, St. Louis, MO, USA
[3]Beckman Institute for Advanced Science and Technology, University of Illinois at Urbana-Champaign, Urbana, IL, USA
[*]vgruev@illinois.edu

Abstract— Despite tremendous developments in preoperative imaging that have enabled physicians to identify cancers with remarkable precision, limited options for intraoperative imaging have left many surgeons ill-equipped to locate tumors in the operating room. Near-infrared fluorescence image-guided surgery has offered to use near-infrared fluorescent dyes and near-infrared sensitive cameras to highlight diseased tissue, but state-of-the-art imaging systems have been unable to provide both the single sensor architecture and the high dynamic range required to facilitate precise surgical procedures under operating room illumination. In seeking a solution, we have monolithically integrated an array of forward-biased photodiodes and an array of interference filters to provide a logarithmic photoresponse across four spectral channels. The resulting single-chip snapshot multispectral imaging system provides an instantaneous dynamic range of >120 dB and a maximum signal-to-noise ratio of ~56 dB across three color channels and one near-infrared channel. Capable of detecting less than 50 nM of the clinically-relevant fluorescent dye indocyanine green, this image sensor offers the high performance required for real-world surgical application.

INTRODUCTION

In the past few decades, tremendous effort has been directed to the development of preoperative imaging technologies. With the conception of computed tomography (CT) and positron emission tomography (PET) in the 1960s and 1970s, anatomic features and metabolic activities could be visualized and tracked as never before. In more recent years, the fusion of CT and PET has permitted scientists to correlate the structure and function of human tissue, and the adoption of magnetic resonance imaging (MRI) has offered physicians more detailed images without ionizing radiation. Despite these advancements, though, intraoperative imaging technologies have been plagued by slow progress. The inclusion of CT, PET, and MRI in the operating room has been hindered by the limited resources available to many hospitals and the great complexity associated with surgical protocols, and the absence of capable alternatives has left many surgeons equipped with little more than their natural senses when identifying and resecting tissue [1].

This disconnect between the capabilities provided by state-of-the-art imaging technologies and the performance required for cutting-edge medical procedures is exemplified in cancer surgery: Due to the low contrast between the tumor boundary and the surrounding tissue, many surgeries end in incomplete resection where cancerous tissue is left in the body, requiring secondary interventions and threatening further complications [2]. Taking advantage of the relative transparency of human tissue in the near-infrared (NIR) spectrum, near-infrared fluorescence (NIRF) image-guided surgery (IGS) utilizes NIR fluorescent dyes and NIR sensitive cameras to label tumors and permit easy verification of complete resection [3], [4]. Extensive work has been aimed at developing NIRF dyes with greater specificities and higher quantum yields [5], but commercial instrumentation for dye detection has been comparatively limited in its advancement [6]. Commercial instruments largely rely on trees of beamsplitters and imagers to separate color images and NIR images, but temperature-dependent co-registration error caused by thermal expansion/contraction in the optical train creates a risk of iatrogenic damage [7]. Single-chip imaging solutions that combine filter arrays and image sensors have enabled spectral separation without introducing co-registration error, but conventional image sensors are unable to provide the dynamic range of >100 dB required to simultaneously image brightly illuminated surgical sites and weakly emitting fluorescent dyes [7], [8]. High dynamic range devices that utilize neuromorphic architectures based on time-domain measurements [9]–[16] or logarithmic architectures constructed around sub-threshold transistors [17]–[22] have been proposed in the literature, but these sensors have not seen application in NIRF IGS. More recently, a high dynamic range image sensor utilizing an asynchronous array of time-domain pixels was evaluated for use in the operating room, but the unique readout scheme from such arrays means that additional work is required to parse the measured timestamps into usable images [23].

In an effort to capture high dynamic range images that remain easily interpretable, we have developed a new imaging system for NIRF IGS that replaces the reverse-biased photodiode in the standard three-transistor pixel with a forward-biased photodiode that exhibits a unique response: It eschews a photovoltage that is linear with light intensity for a photovoltage that is logarithmic. The preservation of the three-transistor pixel ensures that the layout and architecture of this imager can mimic those of conventional imagers, while the transition to a logarithmic response compresses the dynamic range under strong illumination and provides additional sensitivity to weak signals. We have monolithically integrated this logarithmic

This material is based upon work supported by the Air Force Office of Scientific Research under Grant No. FA9550-18-1-0278, the Congressionally Directed Medical Research Programs under Grant No. W81XWH-19-1-0299, and the National Science Foundation under Grant No. 1740737.

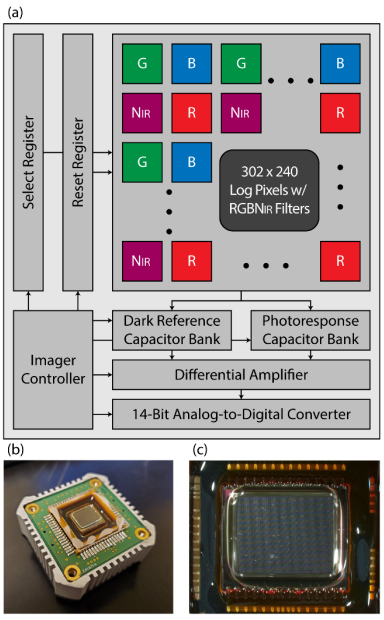

Fig. 1. (a) Block diagram of the sensor's architecture. Arrays of logarithmic pixels and interference filters have been monolithically integrated to provide a high dynamic range and four spectral channels. (b) Photograph of image sensor, integrated filters, and support electronics. (c) Micrograph of image sensor and integrated filter.

image sensor with pixelated interference filters that provide high transmission and high optical densities across four spectral channels—three color channels in the visible spectrum and one broadband channel in the NIR spectrum. This spectral discrimination means that bright surgical scenes and dim fluorescent dyes can be captured at the same time across the same array—eliminating the issues of dynamic range and co-registration error while ensuring a simple and compact device. This single-chip snapshot multispectral imager provides an instantaneous dynamic range of >120 dB and a maximum signal-to-noise ratio of ~56 dB, enabling the detection of the clinically-relevant fluorescent dye indocyanine green at concentrations less than 50 nM.

THE LOGARITHMIC PIXEL

The extraordinary ubiquity of digital cameras can be explained by the existence of simple circuits for converting incident photon fluxes into measurable photovoltages. Contemporary image sensors convert an optical signal into an electrical signal using a reverse-biased photodiode. By permanently connecting the photodiode's anode to the zero potential and temporarily switching its cathode to a positive potential, a reverse bias can be established across the photodiode, and a positive voltage can be stored on the junction capacitance. By subsequently isolating the anode and the cathode from all current loops, the photodiode can be operated as an optoelectronic transducer: As incident photons excite electrons from the valence band to the conduction band, the electrons diffuse into the depletion region, drift away from the anode, and accumulate on the cathode, and the voltage across the junction capacitance decays from a positive value towards zero. The resulting voltage V_{rb} after integration time τ_{int} is

$$V_{rb}(I_{photo,avg}) = V_{rst} - \frac{\tau_{int} I_{photo,avg}}{C_{junc}}$$

where V_{rst} is the reset voltage, $I_{photo,avg}$ is the temporally-averaged photocurrent, and C_{junc} is the junction capacitance [24]. Since the light intensity and the photocurrent are directly proportional in ordinary operation, the reverse-biased photodiode produces a photovoltage that varies linearly with light intensity; to this end, specialized readout architectures can be applied to ensure linearity system-wide [25]–[29].

Despite the prevalence of image sensors constructed with such reverse-biased photodiodes, it is possible to build image sensors in another way using a forward-biased photodiode. By first shorting the photodiode's anode and cathode, a zero bias can be established, and by then breaking the current loop and exposing the photodiode to light, a forward bias can be created: As incident photons excite electrons, the electrons migrate from the anode to the cathode and accumulate on the junction capacitance, causing the voltage to decay from zero towards a negative value. Due to the forward bias from the anode to the cathode, a forward current flows across the photodiode, but since there is no current loop from the anode to the cathode, this forward current must equal the photocurrent. According to the Shockley diode equation, a forward voltage V_{fb} is generated by the forward current and is determined by the logarithmic equation

$$V_{fb}(I_{photo,inst}) = \frac{kT}{q} \ln\left(\frac{I_{photo,inst}}{I_s} + 1\right)$$

where k is the Boltzmann constant, T is the temperature, q is the elementary charge, $I_{photo,inst}$ is the instantaneous photocurrent, and I_s is the saturation current [30]. Consequently, the forward-biased photodiode produces a photovoltage that varies logarithmically with light intensity.

While the reverse-biased photodiode produces electrical signals that preserve the ratio between light intensities and can thus be intuitively understood, the forward-biased photodiode with its non-linear mapping offers its own benefits. For example, the logarithmic relationship between the light intensity and the photovoltage effectively compresses the dynamic range of the imaged scene, enabling high dynamic range imaging without undue constraints on the voltage swing of the readout amplifiers. Furthermore, the logarithmic relationship causes the photovoltage to increase rapidly at low light, increasing sensitivity to small signals and enabling extraction of small variations that otherwise may go undetected. Indeed, the forward-biased photodiode offers key improvements for NIRF IGS where the dynamic range between the visible illumination and the NIR emission is very large and the NIR signal itself is very small. By exploiting the high dynamic range, a single-chip imager can simultaneously measure multiple channels across the visible spectrum and NIR spectrum under surgical illumination, and by utilizing the high sensitivity, weak fluorescent signals can be easily detected.

It can be noted that both the reverse-biased photodiode and the forward-biased photodiode as well as any associated readout circuitry will exhibit mismatches when incorporated into an array. While spatial noise will normally manifest from this

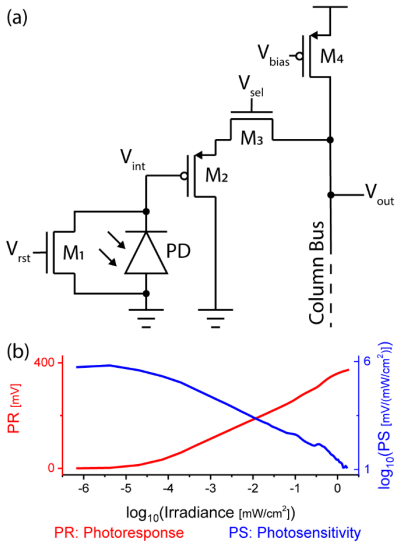

Fig. 2. (a) Electrical schematic of the pixel. By shorting the anode and the cathode of the photodiode during pixel reset, the pixel can be operated in a logarithmic mode. (b) Photoresponse and photosensitivity of the pixel. Except at very low light levels, the photoresponse shows a logarithmic trend that causes the photosensitivity to decrease with light intensity.

variation, such noise can largely be eliminated by using sensing structures that are insensitive to these discrepancies [31]. It can further be reduced with a difference double sampling scheme in which the sensor's photoresponse and its dark response are subtracted; for simplicity, the dark response is often measured during or following a reset operation [32].

THE LOGARITHMIC IMAGE SENSOR

The key difference between the operation of a reverse-biased photodiode and that of a forward-biased photodiode is the biasing condition established during the reset operation. Otherwise, similar circuits are used to measure the photovoltages across the photodiodes, meaning that a linear pixel array and a logarithmic pixel array can be constructed using comparable architectures and layouts [33]. As shown in Fig. 1a, the imaging system is implemented using a rectangular array of logarithmic pixels; select and reset registers at the periphery of the pixel array facilitate the selective readout and reset of each pixel, and a readout chain at the output of the pixel array provides the capacitor banks, differential amplifier, and 14-bit analog-to-digital converter needed to map the analog voltage at each pixel to a digital code that can be transmitted and stored. As shown in Fig. 2a, each logarithmic pixel was designed with a single photodiode and three transistors. The n-well/p-sub photodiode PD and the NMOS reset transistor M_1 provide a logarithmic photovoltage: Prior to exposure, M_1 is enabled so that PD can be zero-biased, and during exposure, M_1 is disabled so that PD can become forward-biased. The PMOS buffer transistor M_2 permits the sensitive photodiode to drive the high-capacitance column bus, and the NMOS select transistor M_3 permits the selective readout of each pixel. The plots of photovoltage and photosensitivity provided in Fig. 2b confirm that the logarithmic pixel provides a logarithmic photoresponse: Except at low light intensities where the limited generation of photocharge causes a breakdown in the simple model of the forward-biased photodiode, the pixel array exhibits a logarithmic relationship between light intensity and

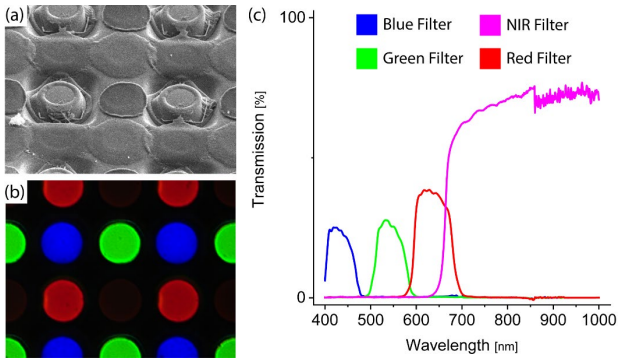

Fig. 3. (a) Scanning electron microscope image of representative pixelated interference filters. (b) White light microscope image of the pixelated interference filters showing the blue, green, red, and near-infrared response. (c) Transmission of each filter.

photovoltage that compresses the dynamic range and provides a high sensitivity to small signals.

To provide spectral discrimination across the visible spectrum and the NIR spectrum, the array of logarithmic pixels was integrated with an array of interference filters capped by absorptive gels. As shown in Fig. 3a and Fig. 3b, a 2-by-2 pixel pattern of interference filters and absorptive gels was used to provide three color channels in the visible spectrum (corresponding to a blue channel, a green channel, and a red channel) and one broadband channel in the NIR spectrum (stretching from 675 nm to well beyond 1000 nm). For each channel, the interference filters were fabricated with different layers of dielectric materials that were deposited using alternating steps of physical vapor deposition. To tune the spectral response of each channel, the number of layers as well as the material and thickness of each layer were selected using iterative optimization in which the transmission was modeled and perturbations were introduced to drive the simulated optical response towards the intended optical response. The interference filters were coated with absorptive gels drawn from commonly used pigments for color filter arrays. This layer provided additional shaping to the transmission spectrum, especially in the visible spectrum. The filter transmissions measured by the fabricator and shown in Fig. 3c indicate that the interference filters and absorptive gels are well matched to color reconstruction and fluorophore detection with lower transmissions matched to bright visible signals and higher transmissions matched to dim NIR signals.

The array of logarithmic pixels was fabricated in a standard 350 nm CMOS process by NIT; the pixels were laid out with a pitch of 15-by-15 µm and a fill factor of 68%. The array of interference filters was fabricated in a custom process by Salvo Technologies; the filters were laid out with a pitch of 30-by-30 µm. Monolithic integration of the pixel array and filter array was completed at the University of Illinois at Urbana-Champaign, resulting in the logarithmic multispectral imaging system shown in Fig. 1b and Fig. 1c. Since the pitches of the arrays differed by a factor of two, the arrays were aligned so that the centers of the filters were coincident with the centers of one subset of pixels and the boundaries between filters were coincident with the centers of the remaining subset of pixels; as a result, the first subset of pixels was completely covered by a

TABLE I. COMPARISON OF RGB-NIR IMAGE SENSORS

	IMEC [35]	ON Semi [36]	PixelTeq [37]	*This Work*
Architecture	CMOS APS	CMOS APS	CCD	*CMOS Log*
Resolution	2.13 MP	2 MP	4 MP	*0.07 MP*
Bitdepth	12 bits	12 bits	Not Listed	*14 bits*
SNR	41.3 dB	41 dB	46.4 dB	*56 dB*
DR	60 dB	75.1 dB	70 dB	*>120 dB*

single type of filter and was retained for images, while the second subset of pixels was covered by multiple types of filters and was discarded from images. This procedure permitted images with a resolution of 302-by-240 pixels.

OPTOELECTRONIC CHARACTERIZATION

In both an ordinary linear pixel with a reverse-biased photodiode and a logarithmic pixel with a forward-biased photodiode, the dynamic range (DR) is limited on the low side by the reset and readout noise; however, the two pixels are limited on the high side by different phenomena. In the case of a linear pixel, the dynamic range is restricted by the supply voltage and the full well capacity, confining the dynamic range of most sensors from 65 dB to 80 dB [8]. In the case of a logarithmic pixel, the dynamic range is theoretically constrained by the maximum open-circuit voltage that can be sustained across the photodiode but is practically bounded by the recombination rate of electron-hole pairs [34]; consequently, the dynamic range is extended to >120 dB. Across a wide variety of light intensities, the signal-to-noise ratio (SNR) maintains a high value, ultimately reaching a maximum value of ~56 dB. The dynamic range and the signal-to-noise ratio of this imaging system and other RGB-NIR imagers are compared in Table 1 ([35]–[37]) where the superiority of the logarithmic architecture over standard architectures can be observed.

Historically, logarithmic image sensors have employed subthreshold transistors to achieve logarithmic mappings from photocurrent to photovoltage; however, subthreshold transistors are highly sensitive to mismatch and are not particularly conducive to calibration—generating a large amount of spatial nonuniformity. Here, though, the logarithmic image sensor with forward-biased photodiodes employs structures that mitigate the effect of mismatch and facilitate the use of difference double sampling; when coupled with optical filters that have been fabricated in an optimized process, the result is low amount of spatial nonuniformity. Indeed, the fixed pattern noise (i.e., the spatial standard deviation normalized to the full dynamic range) did not exceed ~0.6% in any spectral channel of the integrating imaging system as the illuminance was swept over 6 orders of magnitude. This ensures that NIR fluorophores can be consistently identified regardless of location in the surgical site.

NEAR-INFRARED FLUORESCENCE SENSITIVITY

To qualitatively demonstrate the high dynamic range of the logarithmic pixels, a vial of QDot 800, a solution of fluorescent quantum dots that absorbs photons at 780 nm and remits photons at 800 nm, was illuminated from the back by an LED panel and was excited from the side by a 780 nm laser. A shortpass filter that transmits visible light and blocks NIR light was placed in front of the LED panel, and a notch filter that blocks the 780 nm laser was placed in front of the imaging system. This scene exhibited a very large dynamic range between the visible illumination from the LED panel and the fluorescent emission from the quantum dots, providing parallels to conditions in the operating room. As shown in Fig. 4, the imaging system could distinguish the fluorescent signal from the quantum dots despite the background signal from the LED panel, and the NIR information from the vials and the color contents of the scene could be overlaid without co-registration error. Furthermore, the color chart indicates adequate color reproduction, confirming that the image sensor can be used for visually-guided tasks.

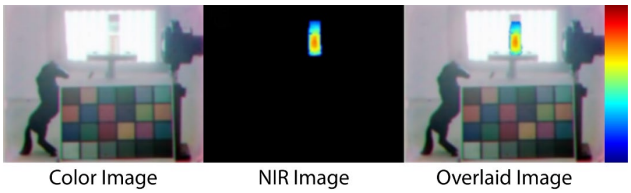

Fig. 4. Sample images showing the high dynamic range capabilites of our logarithmic image sensor across multiple spectral channels. At the top of the scene, a vial of QDot 800 is illuminated by a near-infrared-free LED panel and a near-infrared laser. At the bottom of the scene, a color chart is illuminated by white light. A color image (left), a near-infrared image (center), and an overlaid color/near-infrared image (right) are provided.

To quantitatively determine the fluorescence sensitivity of the logarithmic pixels, the minimal detectable concentration of the fluorescent dye indocyanine green was measured. Three serial dilutions of indocyanine green in deionized water were produced, yielding concentrations from 10 μM to 1 nM, and three samples of deionized water were collected, serving as control data. The samples were excited at a wavelength of 780 nm with an intensity of 20 mW/cm^2 using a filtered and diffused laser and were imaged with the imaging system. The pixel responses from equivalent concentrations were aggregated to minimize error, and the detection limit and the minimal detectable concentration were determined according to the International Union of Pure and Applied Chemistry (IUPAC) standard with a confidence level of 99.86% [38]. Using this method, a minimal detectable concentration of less than 50 nM was established, comparable to similar systems.

CONCLUSION

Although NIRF IGS promises critical information needed to localize tumors during cancer surgery, the limited availability of appropriately designed imaging systems has tempered its acceptance. Imaging systems that incorporate multiple image sensors provide the dynamic range required in the operating room but are accompanied by unpredictable co-registration error, while imaging systems that utilize a single image sensor offer no co-registration error but suffer from an unacceptable dynamic range. To find a solution to these problems, we have combined an array of logarithmic pixels with an array of interference filters to produce a single-chip multispectral imaging system that enables high dynamic range imaging with a cost-effective and space-efficient device free from co-registration error. This sensor has demonstrated an instantaneous dynamic range of >120 dB and a maximum signal-to-noise ratio of ~56 dB, permitting the detection of

clinically-relevant NIRF dyes and paving the way for practical implementations of NIRF IGS.

REFERENCES

[1] S. B. Mondal *et al.*, "Binocular Goggle Augmented Imaging and Navigation System provides real-time fluorescence image guidance for tumor resection and sentinel lymph node mapping," *Sci. Rep.*, vol. 5, no. 1, Jul. 2015.

[2] R. K. Orosco *et al.*, "Positive Surgical Margins in the 10 Most Common Solid Cancers," *Sci. Rep.*, vol. 8, no. 1, p. 5686, Dec. 2018.

[3] A. L. Vahrmeijer, M. Hutteman, J. R. van der Vorst, C. J. H. van de Velde, and J. V. Frangioni, "Image-guided cancer surgery using near-infrared fluorescence," *Nat. Rev. Clin. Oncol.*, vol. 10, no. 9, pp. 507–518, Sep. 2013.

[4] S. B. Mondal, S. Gao, N. Zhu, R. Liang, V. Gruev, and S. Achilefu, "Real-time fluorescence image-guided oncologic surgery," in *Advances in Cancer Research*, vol. 124, Academic Press Inc., 2014, pp. 171–211.

[5] G. Hong, A. L. Antaris, and H. Dai, "Near-infrared fluorophores for biomedical imaging," *Nat. Biomed. Eng.*, vol. 1, no. 1, Jan. 2017.

[6] A. V. DSouza, H. Lin, E. R. Henderson, K. S. Samkoe, and B. W. Pogue, "Review of fluorescence guided surgery systems: identification of key performance capabilities beyond indocyanine green imaging," *J. Biomed. Opt.*, vol. 21, no. 8, p. 080901, Aug. 2016.

[7] M. Garcia, C. Edmiston, T. York, R. Marinov, and V. Gruev, "A Bio-inspired Imager Improves Sensitivity for Near-Infrared Fluorescence Image-Guided Surgery," *Optica*, 2018.

[8] O. Yadid-Pecht and R. Etienne-Cummings, *CMOS Imagers: From Phototransduction to Image Processing*. Springer Science & Business Media, 2007.

[9] C. Posch, D. Matolin, and R. Wohlgenannt, "A QVGA 143 dB dynamic range frame-free PWM image sensor with lossless pixel-level video compression and time-domain CDS," *IEEE J. Solid-State Circuits*, vol. 46, no. 1, pp. 259–275, Jan. 2011.

[10] P. Lichtsteiner, C. Posch, and T. Delbruck, "A 128 x 128 120 dB 15 us Latency Asynchronous Temporal Contrast Vision Sensor," *IEEE J. Solid-State Circuits*, vol. 43, no. 2, pp. 566–576, 2008.

[11] T. Serrano-Gotarredona and B. Linares-Barranco, "A 128 x 128 1.5% Contrast Sensitivity 0.9% FPN 3 µs Latency 4 mW Asynchronous Frame-Free Dynamic Vision Sensor Using Transimpedance Preamplifiers," *IEEE J. Solid-State Circuits*, vol. 48, no. 3, pp. 827–838, Mar. 2013.

[12] E. Culurciello, R. Etienne-Cummings, and K. A. Boahen, "A biomorphic digital image sensor," *IEEE J. Solid-State Circuits*, vol. 38, no. 2, pp. 281–294, Feb. 2003.

[13] A. Kitchen, A. Bermak, and A. Bouzerdoum, "A Digital Pixel Sensor Array With Programmable Dynamic Range," *IEEE Trans. Electron Devices*, vol. 52, no. 12, pp. 2591–2601, Dec. 2005.

[14] C. Shoushun and A. Bermak, "Arbitrated Time-to-First Spike CMOS Image Sensor With On-Chip Histogram Equalization," *IEEE Trans. Very Large Scale Integr. Syst.*, vol. 15, no. 3, pp. 346–357, Mar. 2007.

[15] P. F. Rüedi *et al.*, "A 128 × 128 Pixel 120-dB Dynamic-Range Vision-Sensor Chip for Image Contrast and Orientation Extraction," *IEEE J. Solid-State Circuits*, vol. 38, no. 12, pp. 2325–2333, 2003.

[16] M. Gottardi, N. Massari, and S. A. Jawed, "A 100 µW 128 × 64 Pixels Contrast-Based Asynchronous Binary Vision Sensor for Sensor Networks Applications," *IEEE J. Solid-State Circuits*, vol. 44, no. 5, pp. 1582–1592, 2009.

[17] S. G. Chamberlain and J. P. Y. Lee, "A novel wide dynamic range silicon photodetector and linear imaging array," *IEEE J. Solid-State Circuits*, vol. 19, no. 1, pp. 41–48, 1984.

[18] T. Delbruck and C. A. Mead, "Adaptive photoreceptor with wide dynamic range," in *1994 IEEE International Symposium on Circuits and Systems*, 1994, pp. 339–342.

[19] J. Huppertz, R. Hauschild, B. J. Hosticka, T. Kneip, S. Muller, and M. Schwarz, "Fast CMOS imaging with high dynamic range," in *1997 IEEE Workshop on Charge-Coupled Devices*, 1997.

[20] S. Kavadias, B. Dierickx, D. Scheffer, A. Alaerts, D. Uwaerts, and J. Bogaerts, "A logarithmic response CMOS image sensor with on-chip calibration," *IEEE J. Solid-State Circuits*, vol. 35, no. 8, pp. 1146–1152, Aug. 2000.

[21] M. Loose, K. Meier, and J. Schemmel, "A self-calibrating single-chip CMOS camera with logarithmic response," *IEEE J. Solid-State Circuits*, vol. 36, no. 4, pp. 586–596, 2001.

[22] G. Storm, R. Henderson, J. E. D. Hurwitz, D. Renshaw, K. Findlater, and M. Purcell, "Extended dynamic range from a combined linear-logarithmic CMOS image sensor," *IEEE J. Solid-State Circuits*, vol. 41, no. 9, pp. 2095–2106, 2006.

[23] S. Blair, M. Garcia, N. Cui, and V. Gruev, "A 120 dB, asynchronous, time-domain, multispectral imager for near-infrared fluorescence image-guided surgery," in *2018 IEEE Biomedical Circuits and Systems Conference (BioCAS)*, 2018, pp. 1–4.

[24] J. Nakamura, Ed., *Image Sensors and Signal Processing for Digital Still Cameras*, 1st ed. Boca Raton: Taylor & Francis Group, LLC, 2006.

[25] F. Wang, L. Han, and A. J. P. Theuwissen, "Development and evaluation of a highly linear CMOS image sensor with a digitally assisted linearity calibration," *IEEE J. Solid-State Circuits*, vol. 53, no. 10, pp. 2970–2981, Oct. 2018.

[26] F. Wang and A. J. P. Theuwissen, "Pixel optimizations and digital calibration methods of a CMOS image sensor targeting high linearity," *IEEE Trans. Circuits Syst. I Regul. Pap.*, vol. 66, no. 3, pp. 930–940, Mar. 2018.

[27] V. Gruev, Z. Yang, J. Van Der Spiegel, and R. Etienne-Cummings, "Two transistor current mode active pixel sensor," in *2007 IEEE International Symposium on Circuits and Systems*, 2007, pp. 2846–2849.

[28] R. Njuguna and V. Gruev, "Current-mode CMOS imaging sensor with velocity saturation mode of operation and feedback mechanism," *IEEE Sens. J.*, vol. 14, no. 3, pp. 710–721, Mar. 2014.

[29] T. York *et al.*, "Bioinspired polarization imaging sensors: From circuits and optics to signal processing algorithms and biomedical applications," *Proc. IEEE*, vol. 102, no. 10, pp. 1450–1469, Oct. 2014.

[30] B. E. A. Saleh and M. C. Teich, *Fundamentals of Photonics*, 2nd ed. Hoboken, NJ: Wiley-Interscience, 2007.

[31] Y. Ni, F. Lavainne, and F. Devos, "CMOS Compatible Photoreceptor for High-Contrast Car Vision," in *Proc. SPIE 2344, Intelligent Vehicle Highway Systems*, 1995.

[32] Y. Ni and K. Matou, "A CMOS Log Image Sensor with On-Chip FPN Compensation," in *Proceedings of the 27th European Solid-State Circuits Conference*, 2001.

[33] Y. Ni, Y. Zhu, and B. Arion, "A 768x576 Logarithmic Image Sensor with Photodiode in Solar Cell Mode," Verrières le Buisson, 2011.

[34] R. R. King *et al.*, "Band gap-voltage offset and energy production in next-generation multijunction solar cells," *Prog. Photovoltaics Res. Appl.*, vol. 19, no. 7, pp. 797–812, Nov. 2011.

[35] IMEC, "Snaptshot RGB-NIR multispectral image sensor." [Online]. Available: https://www.imec-int.com/drupal/sites/default/files/inline-files/SNm2x2 snapshot RGB NIR multispectral image sensor.pdf. [Accessed: 03-Nov-2019].

[36] ON Semiconductor, "AR0238: 1/2.7-Inch 2.1 Mp/Full HD Digital Image Sensor," 2017. [Online]. Available: https://www.onsemi.com/pub/Collateral/AR0238-D.PDF. [Accessed: 03-Nov-2019].

[37] PixelTeq, "PixelCam OEM multispectral cameras." [Online]. Available: https://pixelteq.com/wp-content/uploads/2018/02/Ocean-Optics-PixelCam-Flyer.pdf. [Accessed: 03-Nov-2019].

[38] A. D. McNaught and A. Wilkinson, *Compendium of Chemical Terminology*, 2nd ed. Oxford: Blackwell Scientific Publications, 1997.

A 3.47 e$^-$ Read Noise, 81 dB Dynamic Range Backside-Illuminated Multispectral Imager for Near-Infrared Fluorescence Image-Guided Surgery

Steven Blair[1], Amit Deliwala[1], Eric Chen[1], Sailesh Subashbabu[1], Anthony Li[1], Mebin George[1], Missael Garcia[1], Nan Cui[2], Zhongmin Zhu[1], Stefan Andonovski[3], Borislav Kondov[3], Sinisa Stojanoski[3], Magdalena Bogdanovska Todorovska[3], Gordana Petrusevska[3], Goran Kondov[3], Viktor Gruev[1,4,*]

[1]Department of Electrical and Computer Engineering, University of Illinois at Urbana-Champaign, Urbana, IL, USA
[2]Department of Electrical and Systems Engineering, Washington University in St. Louis, St. Louis, MO, USA
[3]Medical Faculty, Saints Cyril and Methodius University in Skopje, Skopje, Republic of North Macedonia
[4]Beckman Institute for Advanced Science and Technology, University of Illinois at Urbana-Champaign, Urbana, IL, USA
[*]vgruev@illinois.edu

Abstract— Near-infrared fluorescence image-guided surgery relies on an interdisciplinary community to develop near-infrared fluorescent markers and near-infrared sensitive cameras capable of mapping relevant structures during surgical procedures. As biochemists pursue a new generation of near-infrared fluorophores aimed at surgical oncology and other applications, optoelectronic engineers developing near-infrared imagers have been slow to adopt architectural improvements that will enhance outcomes in existing operations and to document optoelectronic characteristics that are needed to predict endpoints for new procedures. Here we present a single-chip snapshot multispectral imaging system that integrates arrays of bandpass optical filters and six-transistor backside-illuminated pixels to provide RGB-NIR images with low read noise (3.47 e-) and high dynamic range (81 dB). This imaging system is being used in clinical studies for sentinel lymph node mapping during breast cancer surgery.

INTRODUCTION

As an imaging technique that combines near-infrared fluorescent markers and near-infrared sensitive cameras to map relevant structures during surgical procedures, near-infrared fluorescence (NIRF) image-guided surgery (IGS) has long promised to help surgeons identify tumor margins during cancer surgery [1], [2]. However, the regulatory approval of only two general-purpose fluorophores and the commercial unavailability of tumor-targeted markers have largely limited clinical application to the non-specific visualization of blood vessels and similar structures [3], [4]. The coalescence of biomedical researchers around several promising fluorophores and the organization of serious studies aimed at rapid clinical translation have increased the likelihood that regulators will soon open the flood gates on probe development [5]. Nevertheless, the hesitance of the imaging community to prepare for a prospective market has produced another hurdle to wide-spread adoption: State-of-the-art NIRF IGS imaging systems like the SPY Elite, the Quest Spectrum, and the EleVision IR are released with marketing pamphlets describing prior success with common tasks like perfusion assessment, but medical companies have failed to provide the serious evaluations of system performance required for novel tasks like tumor detection [6]–[8].

The impact of this failure is being felt today: Researchers have already noted that the optical architectures of conventional NIRF IGS instruments are vulnerable to temperature-dependent co-registration error, causing the apparent position of labeled tissues to deviate from the actual position in the surgical site [9]. Researchers have also indicated that the optoelectronic architectures used in co-registration-error-free NIRF IGS instruments have difficulty capturing the large dynamic range between the strong visible lights and the weak fluorescent signals present in the operating room, requiring that surgical lights be dimmed and that surgeons work in the dark [9], [10]. These limitations are not addressed in the publicly-available literature from major companies. Further problems will emerge in the coming years: As surgical protocols for new drugs are designed and implemented, the optimization of fluorophore dosages, fluorescent excitation, and other variables will require knowledge of the read noise, quantum efficiency, and other optoelectronic properties of the imaging system—quantities notably unreported across commercial systems. Lists of architectural choices and optoelectronic characteristics may be unattractive to the decision makers in medical organizations, but they are necessary for the prediction of clinical endpoints in up-and-coming applications.

To establish a new performance baseline for NIRF IGS imaging systems, we have sought to address the architectural shortfalls of existing imaging systems while emphasizing the optoelectronic performance of the next generation of imaging systems. To this end, we have developed a single-chip snapshot multispectral imaging system that combines a scientific CMOS image sensor and a pixelated interference filter array to enable real-time surgical guidance for fluorescently-labeled tissue. A block diagram and assorted pictures of the imaging system are provided in Fig. 1. Monolithic integration of the image sensor with a filter array enables capture of 1024-by-1024-pixel RGB-NIR images with perfect spatiotemporal co-registration, while backside illumination of the image sensor promotes the high quantum efficiencies needed for observing weak fluorescence signals. An image sensor comprised of six-transistor pixels and two readout chains enables a high intrascene dynamic range (81 dB) that is better aligned to the surgical environment in addition

This material is based upon work supported by the Air Force Office of Scientific Research under Grant No. FA9550-18-1-0278, the Congressionally Directed Medical Research Programs under Grant No. W81XWH-19-1-0299, and the National Science Foundation under Grant No. 1740737.

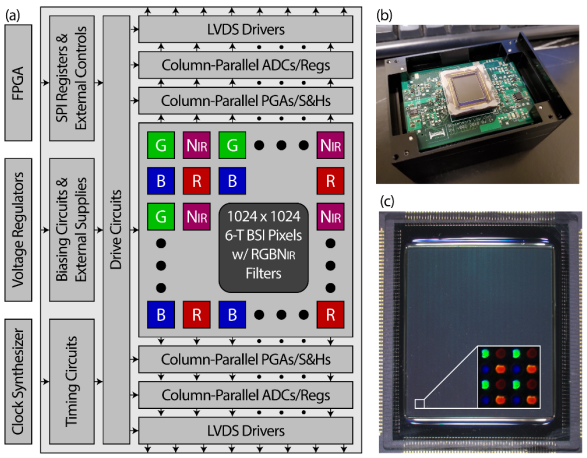

Fig. 1. (a) Block diagram of the imaging system's architecture. Arrays of six-transistor (6-T) backside-illuminated (BSI) pixels and bandpass optical filters have been monolithically integrated to provide low noise, high dynamic range, high quantum efficiencies, and four spectral channels. (b) Photograph of image sensor and integrated filters with support electronics used for control and power. (c) Micrograph of image sensor and integrated filters with transmission microscope image of integrated filters.

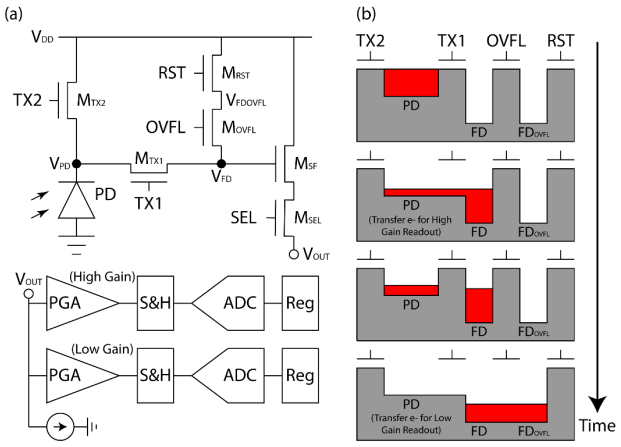

Fig. 2. (a) Schematics of six-transistor pixel and readout chains. (b) Readout process for six-transistor pixel showing charge transfer between photodiode, floating diffusion, and floating diffusion overflow under bright illumination.

to a low read noise (3.47 e^-) that is conducive to the accurate mapping of weakly emitting fluorescent markers. The image sensor is undergoing clinical translation for sentinel lymph node mapping during breast cancer surgery (ClinicalTrials.gov ID: NCT03619967).

DESIGN OF IMAGING SYSTEM

The design of a single-chip snapshot imager for NIRF IGS requires means for spectrally filtering and spatially sampling incident light. For these purposes, we have utilized an array of bandpass optical filters that provide sensitivity in the blue, green, red, and NIR, and an array of six-transistor backside-illuminated pixels that provide low read noise, high dynamic range, and high quantum efficiencies.

Overview of Pixelated Interference Filter Array

The array of bandpass optical filters is constructed from alternating layers of high dielectric constant and low dielectric constant materials, facilitating the reflection of light at the boundary between materials and the interference of light on the transmission side of the stack. With proper selection of the dielectric constants of the materials as well as the number and thickness of the layers, constructive interference inside a spectral band and destructive interference outside the spectral band can be promoted on the transmission side to produce an overall bandpass response for the stack [11]. The stack of dielectric materials is capped by a layer of gels that further shape the transmission spectrum through absorption of unwanted light—especially in the visible spectrum where absorptive pigments have already been optimized for color imaging. After developing a library of bandpass filters aligned to blue, green, red, and NIR wavelengths, the four filters can be deposited in a two-by-two pattern across a glass substrate to facilitate spectral sampling of incident light across a focal plane. This architecture enables the construction of full color images from the blue, green, and red spectral samples and NIR images from the NIR spectral samples.

Overview of Scientific CMOS Image Sensor

A single pixel and the associated readout chain from the array of six-transistor backside-illuminated pixels are depicted schematically in Fig. 2a. Similar to a traditional 5-transistor pixel, M_{TX2} can be used to reset the pinned photodiode, M_{RST} can be used to reset the floating diffusion, M_{TX1} is used to transfer photocharge from the pinned photodiode to the floating diffusion, M_{SF} is used to buffer the photosignal heading to the column bus, and M_{SEL} is used to select the photosignal driving the column bus. A 6th transistor, M_{OVFL}, creates a barrier between the floating diffusion proper and the floating diffusion overflow. When M_{OVFL} is off, the floating diffusion alone has a smaller capacitance that limits the full well capacity but increases the conversion gain, but when M_{OVFL} is on, the combined floating diffusion/floating diffusion overflow has a larger capacitance that increases the full well capacity but limits the conversion gain. The image sensor also contains two readout chains consisting of column-parallel programmable gain amplifiers (PGAs), sample-and-holds (S&Hs), analog-to-digital converters (ADCs), and registers. Amplification and digitization as well as correlated double sampling are facilitated by proper timing of these readout components. One readout chain is setup with a high gain, facilitating readout of a small amount of photocharge on the floating diffusion alone, while the other readout chain is setup with a low gain, facilitating readout of a potentially large amount of photocharge on the combined floating diffusion/floating diffusion overflow.

The design of the image sensor enables rapid readout of high dynamic range scenes at low read noise, but the timing of the individual components of the six-transistor pixel and the readout chains must be carefully controlled. After an exposure, the column circuitry must be reset. First, the columns are reset: By driving RST high and $OVFL$ high in the pixel, any charge from a previous exposure is moved from the floating diffusion and the floating diffusion overflow to the supply rail, and by properly asserting the relevant signals in the readout chains, all capacitances in the PGAs, the S&Hs, and the ADCs are also discharged. Second, the low gain readout chain is initialized: By driving RST low while keeping $OVFL$ high in the pixel, the

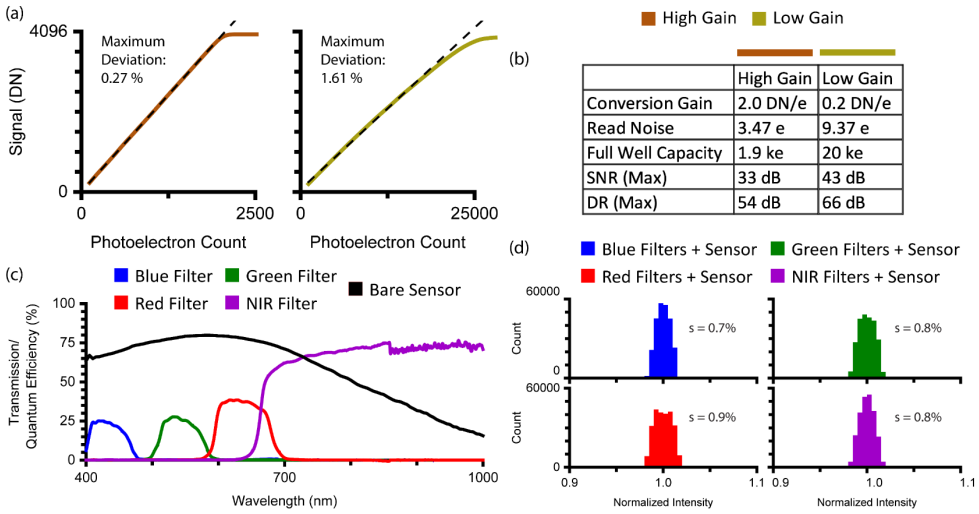

	High Gain	Low Gain
Conversion Gain	2.0 DN/e	0.2 DN/e
Read Noise	3.47 e	9.37 e
Full Well Capacity	1.9 ke	20 ke
SNR (Max)	33 dB	43 dB
DR (Max)	54 dB	66 dB

Fig. 3. (a) Linearity of image sensor. (b) Sensitivity and noise of image sensor. (c) Transmissions for filter array and quantum efficiencies for bare sensor. (d) Fixed pattern noise of high gain channel for integrated filter array and image sensor evaluated at half dynamic range.

floating diffusion and the floating diffusion overflow accumulate a reset charge, and by staggering the deassertion of the resets along the low gain readout chain, the noise voltage from the reset charge can be made the reference voltage in the PGAs, S&Hs, and ADCs [12]. Third, the high gain readout chain is initialized: By keeping RST low while driving $OVFL$ low in the pixel, the floating diffusion samples the reset charge, and by staggering the deassertion of the resets along the high gain readout chain, the noise voltage from the reset charge can be made the reference voltage in the PGAs, S&Hs, and ADCs [12].

At this point, the column readout can begin as indicated by Fig. 2b. First, $TX1$ is pulsed while $OVFL$ remains low so that photocharge is moved onto the floating diffusion, and the resulting voltage is amplified and sampled onto the high gain readout chain. The limited capacitance of the floating diffusions suggests that a full charge transfer may not occur, causing some photocharge to remain on the pinned photodiode [13]. Second, $TX1$ is pulsed while $OVFL$ is pulled high so that photocharge is distributed across the floating diffusion and the floating diffusion overflow, and the resulting voltage is amplified and sampled onto the low gain readout chain. Optimization of the pinned photodiode potential and the floating diffusion/floating diffusion overflow capacitance ensures that a full charge transfer occurs, leaving the photodiode reset for another exposure [14]. Using a ramp ADC, the reset voltage and the signal voltage can be digitized and subtracted, providing additional latitude for offset removal and noise cancellation [15], and finally, the digitized output can be readout via low-voltage differential signaling, permitting high-speed readout of the full array.

CONSTRUCTION OF IMAGING SYSTEM

The construction of the NIRF IGS imaging system called for the incorporation of the arrays of bandpass optical filters and six-transistor backside-illuminated pixels. The pixelated interference filter array was fabricated by Salvo Technologies via an iterative sequence of thin-film deposition and lift-off procedures: For each filter type, a lift-off layer was deposited across a glass substrate and clear apertures were produced where filters were desired before thin-film deposition was used to produce filters across the substrate and thin-film lift-off was used to remove undesired filters [9]. The scientific CMOS image sensor was fabricated by Gpixel using a 180 nm backside-illuminated CMOS image sensor process in which, e.g., the image sensor was formed on the device layer of a silicon-on-insulator substrate before thinning was used to remove the handle layer of the wafer [16]; an additional layer of thick silicon could be bonded to the device layer before removal of the handle layer to provide mechanical support for the integrated circuit [17]. During a post-fabrication process at the University of Illinois at Urbana-Champaign, the filter array and the image sensor were precision aligned and bonded to produce a monolithically integrated imaging system. In each 1024-by-1024 pixel snapshot, this 4-channel camera simultaneously captures a color and an NIR image at both high and low gain.

OPTOELECTRONIC CHARACTERIZATION

The scientific CMOS image sensor's linearity, sensitivity, and noise were evaluated by projecting a spatially-uniform beam of monochromatic light onto the image sensor and observing the statistics of the induced signal as the integration time was varied. The maximum deviation from an ideal pixel normalized to the full dynamic range was evaluated between the observed nonlinear response and a fitted linear model for intensities between 5% and 95% of the dynamic range, and the conversion gain, read noise, full well capacity, signal-to-noise ratio (SNR), and dynamic range (DR) were computed using photon-transfer methods. Fig. 3a shows the response of the image sensor versus the number of accumulated photoelectrons. Despite the complex pixel structure and readout scheme, high linearity was maintained across the dynamic ranges of both the high gain channel and the low gain channel. Indeed, the maximum deviation from ideal performance was observed to be 0.27% for the high gain channel and 1.61% for the low gain channel. Fig. 3b tabulates the conversion gain, read noise, full well capacity, signal-to-noise ratio, and dynamic range of the image sensor. As expected, the high gain channel has a high conversion gain, a low full well capacity of 1.9 ke^-, and a low read noise of 3.47 e^-, appropriate for measuring weak photon fluxes, while the low gain channel has a lower conversion gain, a higher full well

TABLE II. COMPARISON OF RGB-NIR IMAGE SENSORS

	IMEC [18]	ON Semi [19]	PixelTeq [20]	*This Work*
Architecure	CMOS	CMOS	CCD	*CMOS*
Resolution	2.13 MP	2 MP	4 MP	*1 MP*
Bitdepth	12 bits	12 bits	Not Listed	*12 bits*
Read Noise	13 e-	5.7 e-	12 e-	*3.47 e-*
DR	60 dB	75.1 dB	70 dB	*81 dB*

capacity of 20 ke$^-$, and a modest read noise of 9.37 e$^-$, appropriate for measuring strong photon fluxes. Individually, the high gain channel and the low gain channel have dynamic ranges of 54 dB and 66 dB, respectively, but when the channels are fused, a dynamic range in excess of 81 dB can be achieved.

Fig. 3c shows the transmissions for the filter array measured by Salvo Technologies which peak at 25% at 419 nm for the blue channel, 28% at 532 nm for the green channel, 39% at 629 nm for the red channel, and 76% at 859 nm for the NIR channel; it also shows the quantum efficiencies measured by our research group for the bare sensor which peak at 80% at 580 nm. The high transmission enabled by the optimized design of the filter array and the high quantum efficiencies enabled by the backside-illuminated architecture of the image sensor indicate that photons can be collected efficiently, especially in the NIR spectrum. Fig. 3d shows the fixed pattern noise (i.e., the spatial standard deviation over the spatial mean at half dynamic range) for the integrated imaging system which is bound to 0.9% in the high gain channel after gain-offset correction. Such low fixed pattern noise is achieved due to optimizations during the design and fabrication of both the image sensor and the filter array.

Altogether, the optoelectronic performance of the imaging system and the application-specific requirements for the operating room are well matched. The high quantum efficiencies and low noise maximize the probability that sparse fluorescent photons generate a meaningful NIR signal, while the high dynamic range eases the simultaneous capture of weak fluorophores and well-illuminated anatomy. Meanwhile, the low fixed pattern noise and high linearity ensure that NIR signals can be quantitatively evaluated regardless of position and intensity, while the single-chip snapshot architecture ensures that NIR signals and visible images are always co-registered in space and time. This imaging system's optoelectronic performance is superior to or competitive with commercial RGB-NIR imager sensors (Table 1, [18]–[20]), and its combination of features has never been reported in a single imaging system for NIRF IGS to the best of our knowledge.

CLINICAL TRANSLATION

While NIRF IGS cannot be readily applied for tumor detection using available fluorescent markers, NIRF IGS has found relevance in intraoperative cancer staging even with non-specific optical probes. During surgery, the lymph nodes near a cancerous growth are mapped using an NIR dye and an NIR camera (sentinel lymph node mapping) before being surgically removed and histopathologically examined for the presence of a metastasis (sentinel lymph node biopsy). If the biopsy comes back negative, then a more conservative surgical protocol can be followed, reducing the risk of long-term side-effects like lymphadema, but if the biopsy comes back positive, then a more invasive surgical protocol must be used to ensure that the entirety of the cancer is removed [21]. Since mapping and biopsy occur during the cancer surgery and can radically alter the surgical process, there is a strong emphasis on quick mapping procedures with high sensitivity [22].

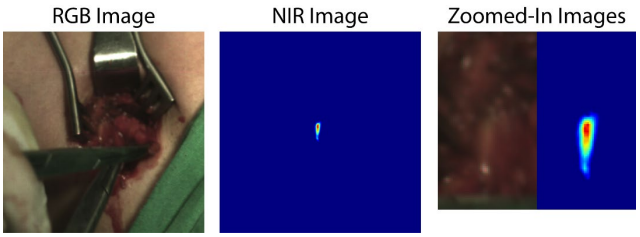

Fig. 4. Sample image of the NIR fluorescence from a sentinel lymph node during a breast cancer surgery. In the left image, the surgical site can be seen in an RGB image, and in the center, the sentinel lymph node can be visualized in an NIR image (with colormap). On the right, a zoomed-in image shows that the lymph node is hard to see in the RGB image but is well demarcated in the NIR image. Both images are perfectly registered.

To explore our NIR fluorescence imaging system's performance for sentinel lymph node mapping, we administered the FDA/EMA-approved NIR fluorophore indocyanine green ($\lambda_{ex} \approx 780$ nm, $\lambda_{em} > 800$ nm) to five women with breast cancer, and we imaged the surgical site during sentinel lymph node mapping and tumor resection. Fig. 4 shows a representative image from the cancer surgery. As can be seen, the visible image provides an intuitive picture of the surgical site, while the NIR image clearly labels the lymph node that is the surgical target. By overlaying the two images, a surgeon can be provided guidance that ensures that they remove the tissue that needs to be removed while avoiding the tissue that shouldn't be removed—easing the job of the surgeon while improving the outcome for the patient. To provide a statistical argument for the superiority of our imaging system over existing imaging systems, larger clinical studies and animal studies like this one are currently being organized and executed.

CONCLUSION

As biochemists seek optimized fluorescent markers for NIRF IGS applications, the imaging community also must seek optimized fluorescence imagers to enable truly impactful clinical applications. However, state-of-the-art imaging systems are released with architectural shortcomings that impair surgical outcomes and are not accompanied with optoelectronic characteristics needed to predict application-specific performance. By monolithically integrating a scientific CMOS image sensor and a pixelated interference filter array, we have developed an NIRF IGS imaging systems that provides high-quality color images and NIR images without spatiotemporal co-registration error. Using an architecture and components optimized for clinical applications, we have simultaneously provided low read noise (3.47 e$^-$), high dynamic range (81 dB), and high quantum efficiencies—features not advertised for commercial systems. Early results from sentinel lymph node mapping during breast cancer surgery indicate that the imaging system is well suited for clinical translation, and on-going analysis continues to probe the relationship between system design and clinical performance.

REFERENCES

[1] T. Ishizawa *et al.*, "Real-time identification of liver cancers by using indocyanine green fluorescent imaging," *Cancer*, vol. 115, no. 11, pp. 2491–2504, May 2009.

[2] S. B. Mondal *et al.*, "Binocular Goggle Augmented Imaging and Navigation System provides real-time fluorescence image guidance for tumor resection and sentinel lymph node mapping," *Sci. Rep.*, vol. 5, no. 1, Jul. 2015.

[3] A. L. Vahrmeijer, M. Hutteman, J. R. van der Vorst, C. J. H. van de Velde, and J. V. Frangioni, "Image-guided cancer surgery using near-infrared fluorescence," *Nat. Rev. Clin. Oncol.*, vol. 10, no. 9, pp. 507–518, Sep. 2013.

[4] S. B. Mondal, S. Gao, N. Zhu, R. Liang, V. Gruev, and S. Achilefu, "Real-time fluorescence image-guided oncologic surgery," in *Advances in Cancer Research*, vol. 124, Academic Press Inc., 2014, pp. 171–211.

[5] G. Hong, A. L. Antaris, and H. Dai, "Near-infrared fluorophores for biomedical imaging," *Nat. Biomed. Eng.*, vol. 1, no. 1, Jan. 2017.

[6] Stryker, "SPY Elite," 2019. [Online]. Available: https://www.stryker.com/us/en/endoscopy/products/spy-elite.html. [Accessed: 25-Oct-2019].

[7] Imaging Quest Medical, "The Quest Spectrum," 2019. [Online]. Available: https://www.quest-mi.com/products.html. [Accessed: 25-Oct-2019].

[8] Medtronic, "EleVision IR Platform," 2019. [Online]. Available: https://www.medtronic.com/covidien/en-us/products/visualization-solutions/elevision-ir-platform.html. [Accessed: 25-Oct-2019].

[9] M. Garcia *et al.*, "Bio-inspired imager improves sensitivity in near-infrared fluorescence image-guided surgery," *Optica*, vol. 5, no. 4, p. 413, Apr. 2018.

[10] O. Yadid-Pecht and R. Etienne-Cummings, *CMOS Imagers: From Phototransduction to Image Processing*. Springer Science & Business Media, 2007.

[11] H. Macleod and H. A. Macleod, *Thin-Film Optical Filters, Fourth Edition*, vol. 20102860. CRC Press, 2010.

[12] A. Krymski, N. Khaliullin, and H. Rhodes, "A 2 e- noise 1.3Megapixel CMOS sensor," in *IEEE Workshop on Charge-Coupled Devices and Advanced Image Sensors*, 2003, pp. 1–6.

[13] X. Wang, B. Wolfs, G. Meynants, and J. Bogaerts, "An 89dB dynamic range CMOS image sensor with dual transfer gate pixel," in *International Image Sensor Workshop 2011*, 2011, pp. 1–4.

[14] C. Ma, Y. Liu, Y. Li, Q. Zhou, X. Wang, and Y. Chang, "A 4-M pixel high dynamic range, low-noise CMOS image sensor with low-power counting ADC," *IEEE Trans. Electron Devices*, vol. 64, no. 8, pp. 3199–3205, Aug. 2017.

[15] Y. Chen, Y. Xu, A. J. Mierop, and A. J. P. Theuwissen, "Column-parallel digital correlated multiple sampling for low-noise CMOS image sensors," *IEEE Sens. J.*, vol. 12, no. 4, pp. 793–799, Apr. 2012.

[16] G. Meynants, J. Bogaerts, X. Wang, and G. Vanhorebeek, "Backside illuminated global shutter CMOS image sensors," in *International Image Sensor Workshop 2011*, 2011, pp. 1–4.

[17] B. Pain, "Backside illumination technology for SOI-CMOS image sensors," in *IISW Symposium on Backside Illumination of Solid-State Image Sensors 2009*, 2009, pp. 1–45.

[18] IMEC, "Snaptshot RGB-NIR multispectral image sensor." [Online]. Available: https://www.imec-int.com/drupal/sites/default/files/inline-files/SNm2x2 snapshot RGB NIR multispectral image sensor.pdf. [Accessed: 03-Nov-2019].

[19] ON Semiconductor, "AR0238: 1/2.7-Inch 2.1 Mp/Full HD Digital Image Sensor," 2017. [Online]. Available: https://www.onsemi.com/pub/Collateral/AR0238-D.PDF. [Accessed: 03-Nov-2019].

[20] PixelTeq, "PixelCam OEM multispectral cameras." [Online]. Available: https://pixelteq.com/wp-content/uploads/2018/02/Ocean-Optics-PixelCam-Flyer.pdf. [Accessed: 03-Nov-2019].

[21] J. J. Albertini *et al.*, "Lymphatic mapping and sentinel node biopsy in the patient with breast cancer," *JAMA J. Am. Med. Assoc.*, vol. 276, no. 22, p. 1818, Dec. 1996.

[22] X. Zhang *et al.*, "Diagnostic performance of indocyanine green-guided sentinel lymph node biopsy in breast cancer: A meta-analysis," *PLoS One*, vol. 11, no. 6, p. e0155597, Jun. 2016.